Journal of Wind Engineering & Industrial Aerodynamics 207 (2020) 104373

Contents lists available at ScienceDirect

Journal of Wind Engineering & Industrial Aerodynamics

journal homepage: www.elsevier.com/locate/jweia

A general-purpose analytical model for reconstructing the thunderstorm outflows of travelling downbursts immersed in ABL flows

Andi Xhelaj *, Massimiliano Burlando, Giovanni Solari

Department of Civil, Chemical and Environmental Engineering, Polytechnic School, University of Genoa, Via Montallegro 1, 16145, Genoa, Italy

ARTICLE INFO

Keywords:
ABL background wind
Downburst analytical model
Downburst geometrical parameters
Downburst kinematic parameters
Stationary downburst
Travelling downburst

ABSTRACT

A "downburst" is defined as a diverging wind system that occurs when a strong downdraft induces an outflow of damaging winds on or near the ground. Severe wind damage in many parts of the world are often due to thunderstorm outflows and their knowledge is therefore relevant for structural safety and design wind speed evaluation. Nevertheless, there is not yet a shared model for thunderstorm outflows and their actions on structures. In this paper, an analytical model that simulates the horizontal mean wind velocity originated from a travelling downburst is proposed. The horizontal wind velocity is expressed as the vector summation of three independent components: the stationary radial velocity generated by an impinging jet over a flat surface, the downdraft translating velocity, which corresponds to the parent cloud motion, and the boundary layer background wind field at the surface where the downburst is immersed. A parametric analysis is also developed and coupled with the analytical model aiming to investigate two observed downburst events and extract their main parameters – e.g. downdraft diameter, touch-down position, translating downdraft speed and direction, intensity and decay period - in order to reconstruct the space-time evolution of these events and validate the model itself.

1. Introduction

The European wind climate and that of many countries at the mid-latitudes is dominated by extra-tropical cyclones and thunderstorms (Letchford et al., 2002). The polar front theory (Bjerknes and Solberg, 1922) explains and describes the genesis and life cycle of extra-tropical cyclones. These are synoptic phenomena that develop in a few days on a few thousand kilometers. In extra-tropical cyclones, far from frontal areas, the velocity field near the ground surface is characterized by a logarithmic mean wind profile within the atmospheric boundary layer (ABL), whose depth is on the order of magnitude of 1–3 km. Here, within time intervals between 10 min and 1-h, turbulent fluctuations are stationary and Gaussian. Davenport (1961) identified the most intense wind events with the extra-tropical cyclones and introduced a model, based on this hypothesis, to determine the wind loading of structures. Over half a century, Davenport's model is still a foundation of wind engineering (Solari, 2019).

The modern study of thunderstorms started when Byers and Braham (1949) proved that these events are mesoscale phenomena that develop over a few kilometers. They consist of convective cells arranged either randomly, in squall-lines or mesoscale convective systems. In each cell, a process lasting approximately 30 min evolves in three stages in which an updraft of warm air is followed by a downdraft of cold air. Starting from these findings, in the 1970's and 1980's Fujita gave key contributions to the knowledge of thunderstorms and their scales (Fujita 1981, 1985; Fujita and Wakimoto, 1981, 1990), showing that the downdraft that impacts the ground surface produces an intense radial outflow and ring vortices as shown in Fig. 1. He called the whole set of these air movements "downburst" and divided these phenomena into "macroburst" and "microburst" depending on whether the outflow diameter (i.e. area of strong winds at the ground surface produced by the downdraft) is greater or smaller than 4 km, respectively (Fujita, 1985). Fig. 2 shows the record of an extreme horizontal wind velocity due to a radial outflow; it exhibits apparent non-stationary properties and reaches about 67+ m s^{-1} at 4.9 m of height above the ground (Fujita, 1990). The rapid passage of the gust front often enhances the destructive effects of this phenomenon.

In the same period in which atmospheric sciences discovered downbursts, giving rise to a huge research effort to understand and explain their properties, wind engineering realized that design wind speed and severe wind damage are often due to thunderstorm outflows and they have a focal role in structural safety (Letchford et al., 2002). Hence, a striking research arose also in this field (Solari, 2014, 2020).

* Corresponding author.
E-mail address: andi.xhelaj@edu.unige.it (A. Xhelaj).

https://doi.org/10.1016/j.jweia.2020.104373
Received 17 April 2020; Received in revised form 30 August 2020; Accepted 30 August 2020

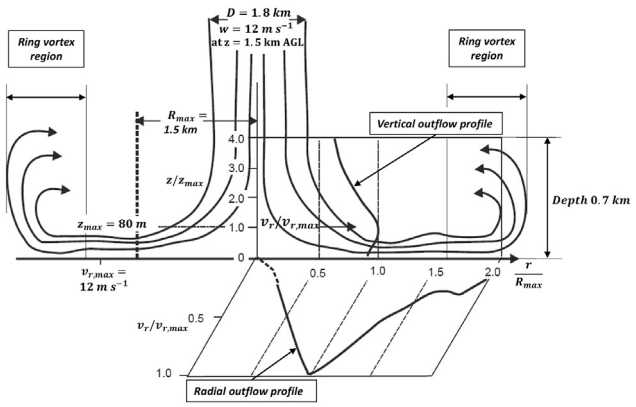

Fig. 1. Structure of a thunderstorm downburst at maximum intensity, vertical, radial outflow profile and vortex region (adapted from Hjelmfelt, 1988).

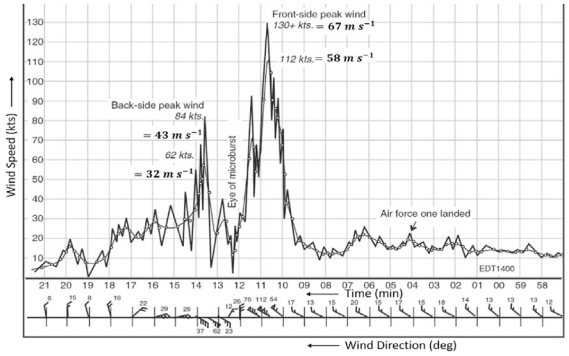

Fig. 2. Recorded and smoothed wind speed and wind direction for Andrews A.F.B. downburst (August 01, 1983) (adapted from Fujita, 1985).

Fig. 3. WP and WPS monitoring network used in this study. Geographic coordinates of the anemometers and their characteristics are reported in Table 1.

Despite this reality, this matter is still affected by huge uncertainties and a shared model of downburst outflows and their actions on structures like the one formulated by Davenport (1961) for synoptic cyclones is not available yet. This happens because the complexity of thunderstorms makes it difficult to establish physically realistic and simple models of these phenomena. Their short duration and small size make a limited amount of thunderstorm data available. Downburst associated loads, diversely from synoptic winds, depend on a variety of parameters such as the diameter of the downdraft, the relative position between the centre of the downburst and the structure, the translation velocity of the parent storm cell and so on. These aspects make the assessment of downburst wind loads very complex. This requires formulating simplified analytical or empirical models, able to capture their main features.

The first analytical models, which were derived from the application of the basic fluid dynamic equations to stationary flows with the aim of obtaining simple expressions, independent of time, of the vertical and radial components of the wind velocity, were the impinging wall jet and the vortex ring model. The impinging wall jet model originated from Glauert (1956), who formulated the theory of the plane radial jet, both laminar and turbulent, without any regard for downbursts; in the case of the laminar jet, he derived a complex analytical solution; in the case of the turbulent jet, the solution is even more complex and controversial and gave rise to a wide scientific debate and to numerous simplified solutions (Xu and Hangan, 2008). The ring vortex model was firstly introduced by Ivan (1986), who developed an axisymmetric model of the downburst, calibrated on the data of the Joint Airport Weather Studies (JAWS) Project (Fujita, 1985; McCarthy et al., 1982); this model considered a primary vortex above the ground and its mirror image, ensuring the boundary condition that the ground plane is a stream surface. The ring vortex stream function was obtained from Lamb (1895).

Oseguera and Bowles (1988) presented the first three-dimensional model of the downburst, later modified by Vicroy (1991). The solution is based on the Euler and continuity equations for an axisymmetric flow around a point of stagnation, involving the use of shape functions that satisfy the results of the TASS (Terminal Area Simulation System) model, formulated by Proctor (1987a, b) using the results of the JAWS Project, laboratory tests carried out through the impinging jet technique on a flat surface, and the outcome of the Northern Illinois Meteorological Research on Downburst (NIMROD) Project (Fujita, 1985; Fujita, 1978).

The analytical and empirical models developed by the above authors were compared by Vicroy (1992). He considered three downburst models, namely a linear model of downburst based solely on the mass conservation constraint, the empirical model by Oseguera and Bowles (1988), as modified by Vicroy (1991), and the ring vortex model by Ivan (1986), later modified by Schultz (1990). He concluded that the last two models gave similar result, but the empirical model was simpler than the ring vortex model.

Later on, Wood and Kwok (1998) and Wood et al. (2001) formulated an empirical model of the vertical profile of the radial wind speed of the downburst calibrated by means of laboratory tests and CFD simulations, which had great success especially in wind engineering applications.

Holmes and Oliver (2000) reconsidered the impinging jet model, providing a simplified expression of the radial component of the mean wind velocity as a function of the distance from the jet axis and the time elapsed from the beginning of the downburst. They also recognized, for the first time in a model, the importance to express the horizontal mean wind velocity as the vector composition of the stationary radial speed produced by the downburst outflow and the translation or background speed of the downburst itself. It is worth noting, however, that this paper does not seem to provide a clear distinction between the low-level environmental flow in the ABL and the motion of the thunderstorm cell.

Li et al. (2012) and Abd-Elaal et al. (2013a) proposed analytical models of the vertical and radial profiles of the horizontal and vertical

Table 1
Main characteristics of the events considered and properties of the monitoring network.

Location	Date	Hour (HH:MM:SS)	Anemometer Code	Geographical Coordinates(λ, ϕ) (°N, °E)	Height AGL (m)	v_{max} (m/s)	$\bar{v}_{max}$ (m/s)	α (deg)
La Spezia	April 11, 2012	07:20:00 07:10:00	SP.02 SP.03	(44.110, 9.839) (44.097, 9.858)	10	32	23	195
					13	24	19	224
Genoa	30 Sept. 2012	21:00:00	GE.02	(44.418, 8.777)	13.3	22	17	163

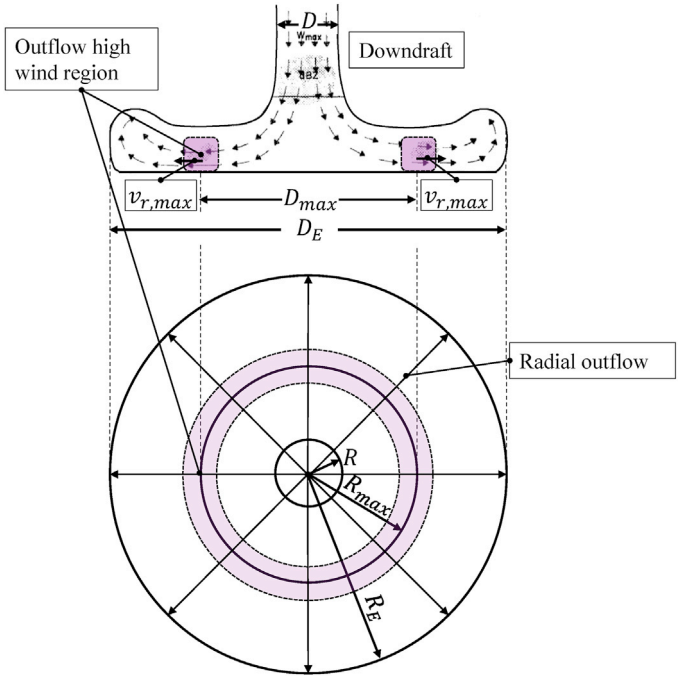

Fig. 4. Schematic view of a stationary downburst and outflow structure parameters. The horizontal wind velocity at height z AGL is characterized by radially symmetric streamlines with an annular ring of high winds (Adapted from Hjelmfelt, 1988).

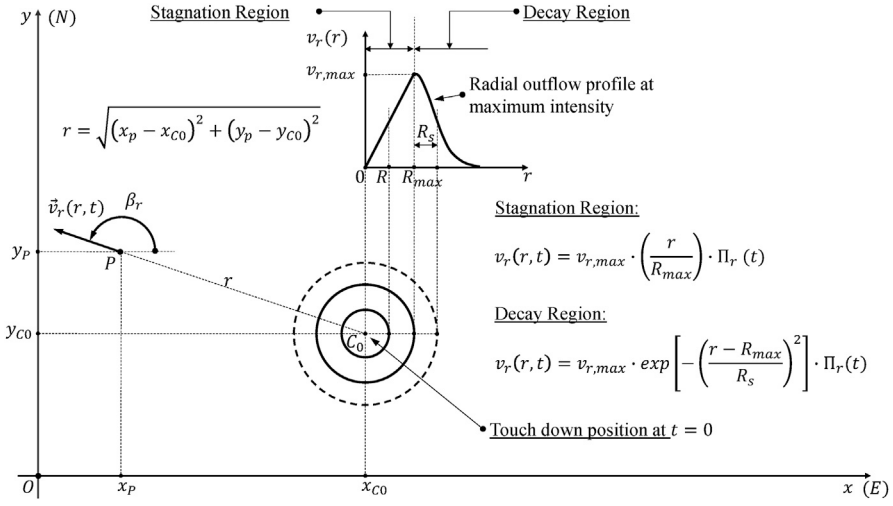

Fig. 5. Schematic view of a spatially stationary downburst.

components of the wind velocity that took into account the nonlinear growth of the surface boundary layer through shape functions derived from CFD simulations. Abd-Elaal et al. (2013b) observed that the difference between downburst recordings often depended on the position and the time in which the downdraft touch-down occurred and its translation speed and direction. Starting from this premise, they implemented a coupled parametric-CFD model whose parameters, obtained from measurements by means of an optimization procedure, allowed reconstructing the space-time evolution of downbursts.

Le and Caracoglia (2017) examined the thunderstorm-induced dynamic response of a reference benchmark tall building subjected to the Andrew Air Force Base (AFB) thunderstorm. The horizontal mean wind velocity at any point of the field was reconstructed by the vector summation of the radial wind velocity and the constant horizontal translation velocity assumed to coincide with the environmental wind field surrounding the downburst. The radial wind velocity at the maximum intensity was assumed as the product of two shaping functions, namely the radial and the vertical shaping function. The Holmes and Oliver model were used to describe the radial shaping function while two different wind profile were used to describe the vertical profile of the (spatially) stationary downburst, namely, the Oseguera-Bowles-Vicroy's model (Oseguera and Bowles, 1988; Vicroy, 1992) and the Wood et al.'s model (2001). It was observed that the Wood et al.'s model is more appropriate when the maximum radial velocity is located near the ground, whereas the Oseguera – Bowles - Vicroy's model is better for maximum radial velocity at higher elevations. They highlighted that the choice of the vertical wind profile is crucial since it can induce extremely unfavourable loading conditions. In the wake of this model, Le and Caracoglia (2018), explored the implementation of the wavelet-Galerkin approach to examine the fragility of vertical structures subjected to thunderstorm downburst wind loads. Wind load error propagation and random variability were incorporated and simulated through

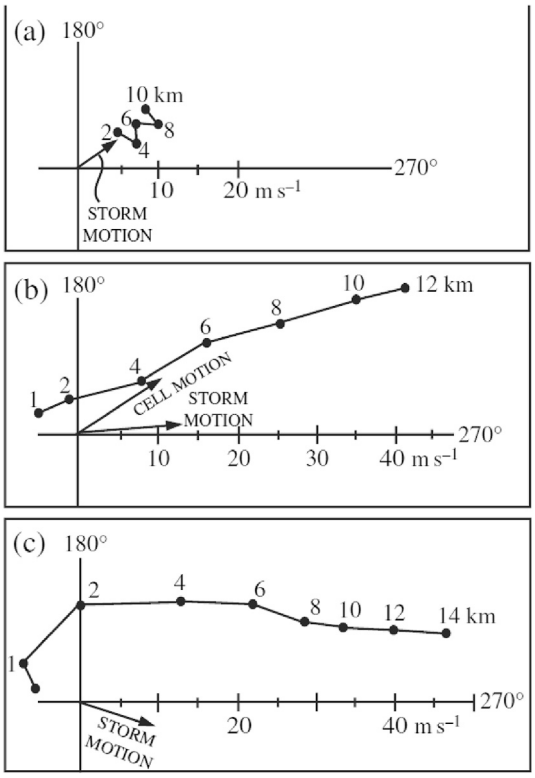

Fig. 6. Typical changes of environmental wind speed and direction with height (hodographs) observed during the Alberta Hail Studies project for (a) single-cell, (b) multicell, and (c) supercell storms. (From Chisholm and Renick, 1972).

Monte-Carlo sampling approach. Various intensity measures were proposed to uniquely define the main features of a downburst. They identified two main parameters to represent load intensity that have a major importance in structural response, namely the maximum radial velocity associated with the Vicroy (1992) horizontal wind profile and the absolute value of the touchdown or initial position of the downburst relative to the centre of mass of the structure.

Jesson and Sterling (2018) formulated a parametric-analytical model of the downburst; it was inspired by the Ivan (1986) and Schultz (1990) models with the addition of a secondary vortex and their temporal variability. The downburst, presented as non-translating (or

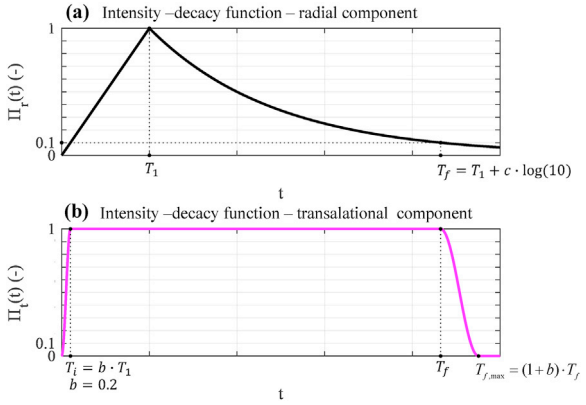

Fig. 8. (a) Intensity-decay function, radial component $\Pi_r(t)$; **(b)** Intensity decay-function, translational component $\Pi_t(t)$.

Table 2
Model parameters.

1	Maximum radial velocity	$v_{r,max}$
2	Downdraft radius	R
3	Period of linear intensification (Π_r)	T_1
4	Duration of the downburst event	T_f
5	x-component touchdown location (at $t = 0$)	x_{C0}
6	y-component touchdown location (at $t = 0$)	y_{C0}
7	Downburst translational velocity	v_t
8	Downburst translational direction	β_t or α_t Eq. (16)
9	Low-level ABL wind speed	v_b
10	Low-level ABL wind direction	β_b or α_bEq. (16)

Table 3
Fixed model parameters.

1	Radial length scale	$R_s = R$
2	Radial distance from downburst centre at which $v_{r,max}$ occurs	$R_{max} = 2 \cdot R$
3	Radial extension of the outflow edge	$R_E = 2 \cdot R_{max} = 4 \cdot R$
4	Parameter of the auxiliary function Δ	$R_{E,max} = (1 + a) \cdot R_{max}$; $a = 0.2$
5	Parameter of the intensity-decay function Π_t	$T_i = b \cdot T_1$; $b = 0.2$
6	Parameter of the intensity-decay function Π_t	$T_{f,max} = (1 + b) \cdot T_1$; $b = 0.2$

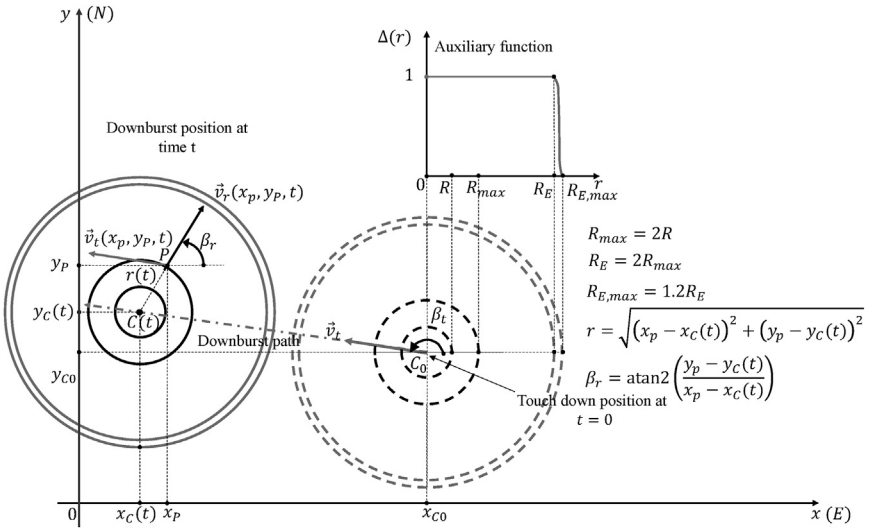

Fig. 7. Schematic representation of the translating downburst.

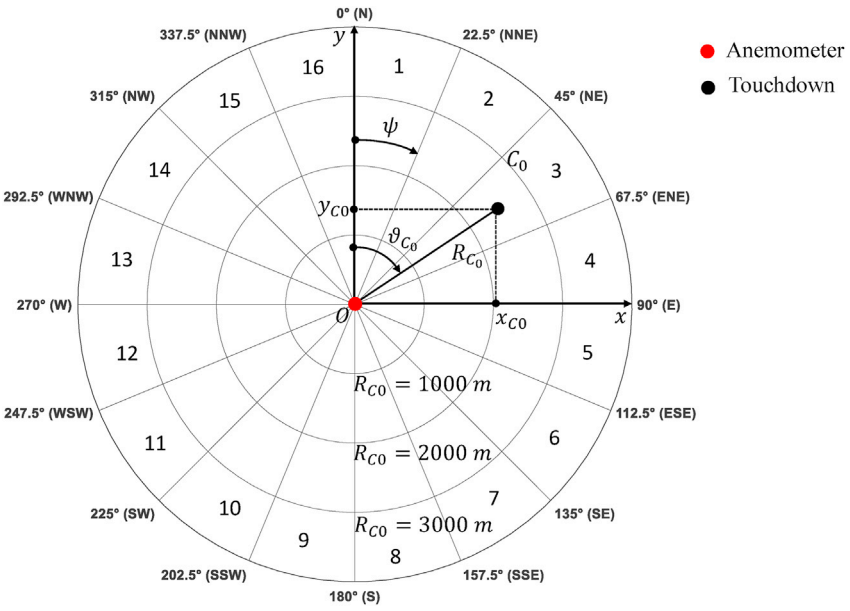

Fig. 9. Parametric analysis phase (*I*); division of the simulation domain in 16 sectors.

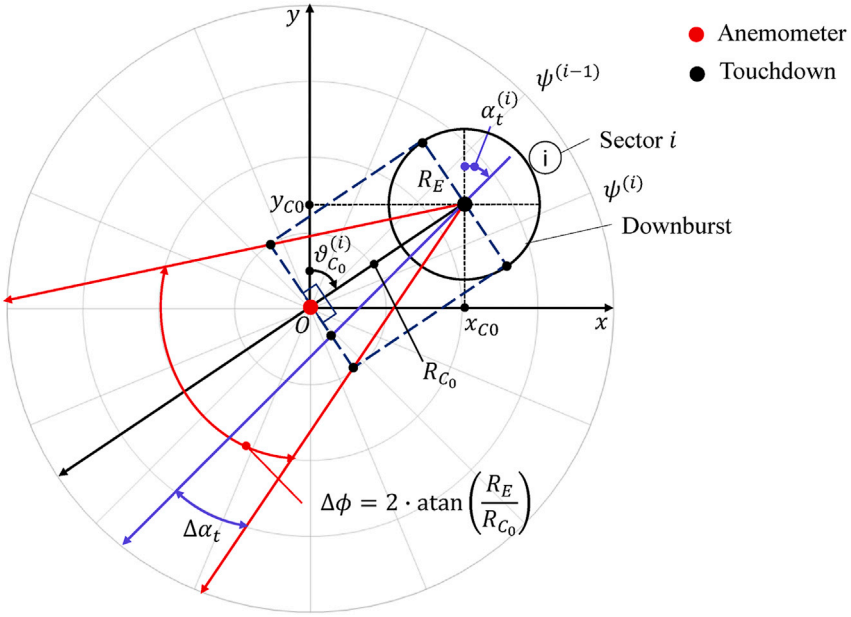

Fig. 10. Parametric analysis phase (*I*); evaluation of the downburst path from the *i*-th sector.

Table 4
Parametric analysis Phase (I); variation range of the eight parameters, step increment $\Delta(I)$, number of values given to each parameter and total simulation number for the i-th sector.

	Parameters (I)	*Min value* (I)	*Increment* $\Delta(I)$	*Maxvalue* (I)	*N° value*(I)
1	$v_{r,max}(I)$ (m/s)	10	8	34	4
2	$R(I)$ (m)	100	150	1000	7
3	$T_1(I)$ (min)	5	10	25	9 ($T_1 + T_f$, $T_1 < T_f$)
4	$T_f(I)$ (min)	10	15	55	
5	$R_{C_0}(I)$ (m)	500	500	8000	16
6	$\vartheta_{C_0}^{(i)}(I)$ (°)	$\psi^{(i-1)} = (i-1)\cdot\Delta\psi$	$\frac{\Delta\psi}{3} = 7.5$	$\psi^{(i)} - \frac{\Delta\psi}{3} = i\cdot\Delta\psi - \frac{\Delta\psi}{3}$	3
7	$\alpha_t^{(i)}(I)$ (°)	$\vartheta_{C_0}^{(i)}(I) - \Delta\varphi/2$	$\Delta\varphi/6$	$\vartheta_{C_0}^{(i)}(I) - \Delta\varphi/2$	7
8	$v_t(I)$ (m/s)	4	4	16	4
Total N° of simulations for the i-th sector =					338 688

Table 5
Parametric analysis Phase (II); variation range of the eight parameters, step increment $\Delta(II)$, number of values given to each parameter and total simulation number.

	Parameters (II)	*Min value* (II)	*Increment* $\Delta(II)$	*Max value* (II)	N° *value*(I)
1	$v_{r,max}(II)$ (m/s)	${v_{r,max}}^*(I) - \Delta v_{r,max}(I)/2$	$\Delta v_{r,max}(I)/5$	${v_{r,max}}^*(I) + \Delta v_{r,max}(I)/2$	6
2	$R(II)$ (m)	$R^*(I) - \Delta R(I)/2$	$\Delta R(I)/5$	$R^*(I) + \Delta R(I)/2$	6
3	$T_1(II)$ (min)	${T_1}^*(I) - \Delta T_1(I)/2$	$\Delta T_1(I)/5$	${T_1}^*(I) + \Delta T_1(I)/2$	6
4	$T_f(II)$ (min)	${T_f}^*(I) - \Delta_f(I)/2$	$\Delta T_f(I)/5$	${T_f}^*(I) + \Delta T_f(I)/2$	6
5	$R_{C_0}(II)$ (m)	${R_{C_0}}^*(I) - \Delta R_{C_0}(I)/2$	$\Delta R_{C_0}(I)/5$	${R_{C_0}}^*(I) + \Delta R_{C_0}(I)/2$	6
6	$\vartheta_{C_0}(II)$ (°)	${\vartheta_{C_0}}^*(I) - \Delta\vartheta_{C_0}(I)/2$	$\Delta\vartheta_{C_0}(I)/5$	${\vartheta_{C_0}}^*(I) + \Delta\vartheta_{C_0}(I)/2$	6
7	$\alpha_t(II)$ (°)	${\alpha_t}^*(I) - \Delta\alpha_t(I)/2$	$\Delta\alpha_t(I)/5$	${\alpha_t}^*(I) + \Delta\alpha_t(I)/2$	6
8	$v_t(II)$ (m/s)	${v_t}^*(I) - \Delta v_t(I)/2$	$\Delta v_t(I)/5$	${v_t}^*(I) + \Delta v_t(I)/2$	6
Total N° of simulations for Phase (II) =					$6^8 = 1\,679\,616$

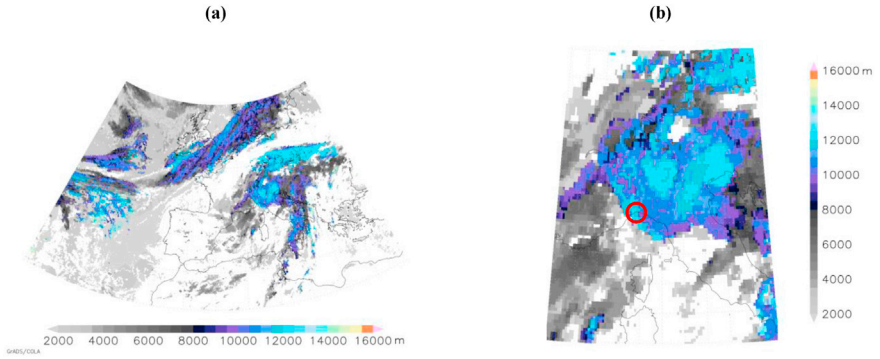

Fig. 11. (a) Large-scale cloud top height distribution from Meteosat Second Generation (MSG) data acquired by Eumetsat, valid for September 30, 2012 at 21:00 UTC. **(b)** Local-scale cloud top height distribution from MSG data for central and northern Italy. The red circle shows the position of the city of Genoa.

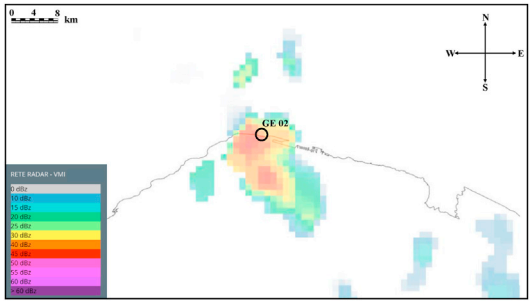

Fig. 12. Composite radar reflectivity (dBZ, vertical maximum intensity) for September 30, 2012 at 21:00 UTC. The black circle indicates the position of the anemometer GE.02 in the harbour of Genoa Voltri.

Table 6
Abrupt change analysis in the standard deviation for the Genoa downburst event of September 30, 2012.

	Anemometer GE 02
v_b^-	2.3 m/s
α_b^-	40°
v_{max}	17 m/s
α_{max}	159°
Δt_{II}	377 s $\simeq$ 6 min
Δt_{III}	579 s $\simeq$ 10 min
$\Delta t_{tot} = \Delta t_{II} + \Delta t_{III}$	956 s $\simeq$ 16 min
v_b^+	3 m/s
α_b^+	53°

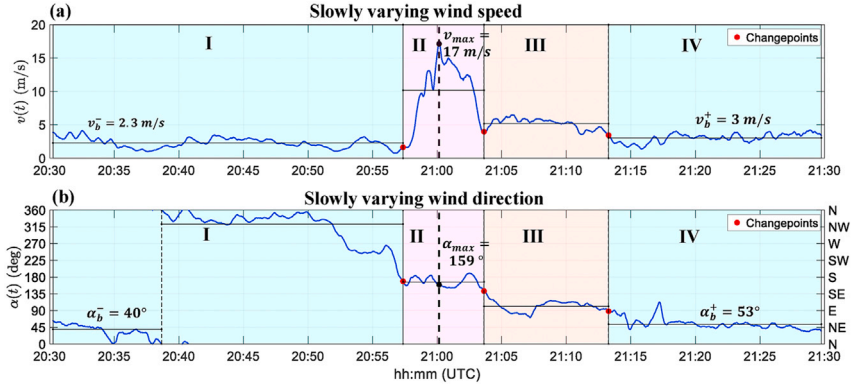

Fig. 13. Genoa monitoring network from 20:30 to 21:30 UTC on September 30, 2012 recorded by the anemometer GE 02: **(a)** slowly varying v ; **(b)** slowly varying mean wind direction α. The vertical long-dashed black line in the centre of the figures shows approximately the passage of the downburst event.

Table 7
Parameters for the simulation of Genoa Downburst, September 30, 2012.

1	$v_{r,max}$	20.4 m/s	Maximum radial velocity
2	R	265 m	Downdraft radius
3	T_1	1440 s	Period of linear intensification of the intensity-decay function (Π_r)
4	T_f	2670 s	Duration of the downburst event (Π_r)
5	x_{C_0}	−3004.5 m	Initial location along the x axis of the touch-down ($t = 0$)
6	y_{C_0}	−1481.7 m	Initial location along the y axis of the touch-down ($t = 0$)
7	v_t	2 m/s	Downburst translation speed
8	α_t	250.2°	Downburst translation direction
9	v_b	2.65 m/s	Low – level ABL wind speed
10	α_b	49°	Low – level ABL wind direction

spatially-stationary), creates a 2-D axially symmetric outflow around the impingement point, thus the variation occurs along the radial and vertical directions only. The wind speed is modelled as the superposition of three independent velocity fields, namely the main outflow from the downdraft impingement point, the primary ring vortex and the secondary vortex. The model was calibrated through laboratory tests and CFD simulations (Mason et al., 2009).

An essential aspect already highlighted with regard to the Holmes and Oliver model (2000), and then repeated in other subsequent papers (Chay at al. 2006, Abd-Elaal et al., 2013b, and Le and Caracoglia (2017)), is the lack of a clear distinction between the translational movement of the thunderstorm cell and the boundary layer wind in which the thunderstorm outflow is immersed at the ground. It is probable that these two phenomena are correlated with each other, but no reason exists, based upon current knowledge, to identify them a priori. It is worth

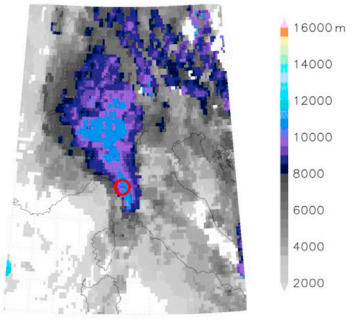

Fig. 16. Cloud top height distribution from Meteosat Second Generation (MSG) data acquired by Eumetsat, valid for April 11, 2012 at 08:00 UTC. The red circle shows the position of La Spezia.

mentioning, however, that Ponte and Riera (2007), Miguel et al. (2018) and (Riera, 2019) argued that the most critical situations for the estimation of the wind excitation on buildings and structures occur when downbursts are generated during the passage of squall lines. The above references make the simplified assumption that the squall lines that cause downbursts are carried by a fully developed extratropical cyclone, which causes the wind in the ABL as well. In this case, downburst translation velocity and direction coincide with the low-level wind velocity and direction in the ABL.

Squall lines are the most common type of mid-latitude severe storms that cause downbursts and usually can be found in the warm sector of an extratropical cyclone (pre-frontal squall lines) or embedded in the cold front of an extratropical cyclone (frontal squall line). However, for all

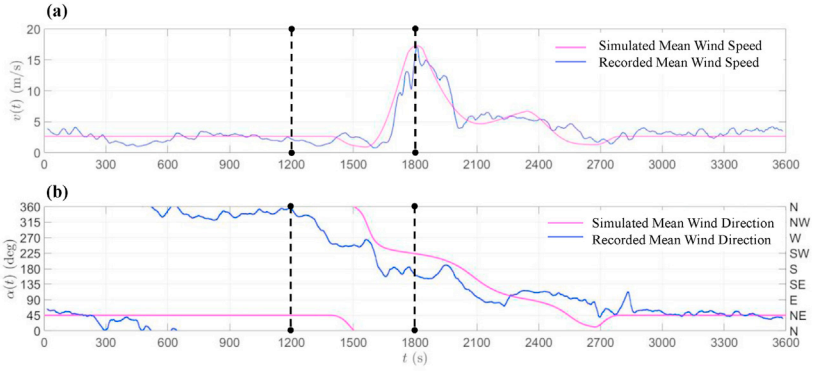

Fig. 14. Simulation of the Genoa Downburst, September 30, 2012. Comparison between the simulated and recorded mean wind speed **(a)** and simulated and recorded mean wind direction **(b)**.

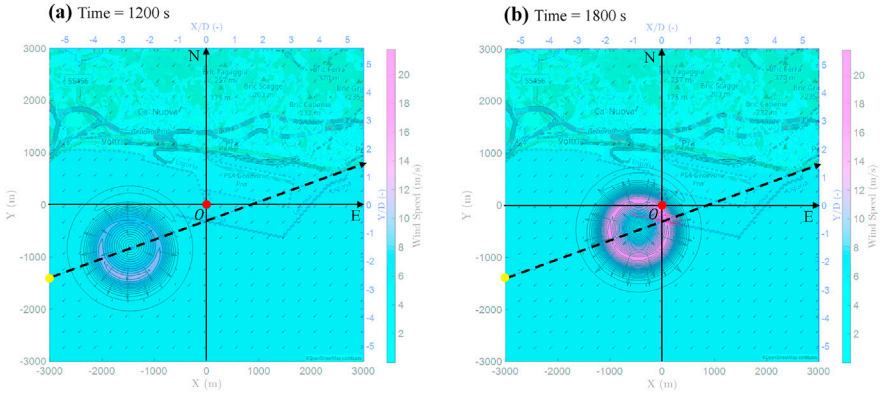

Fig. 15. Simulation of Genoa Downburst, September 30, 2012. **(a)** simulation time = 1200 s; **(b)** simulation time = 1800 s. The red dot indicates the position of the anemometer GE 02 and coincides with the origin O of the reference frame, the yellow dot indicates the touch-down position of the downburst. The black dashed line indicates the downburst path.

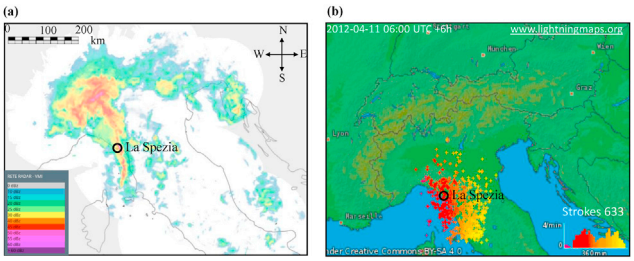

Fig. 17. (a) Composite radar reflectivity (dBZ, vertical maximum intensity) for April 11, 2012 at 08:00 UTC. Estimated rainfall increases by about a factor of five from the faintest echoes, rendered in blue, to the strongest echoes rendered in magenta. **(b)** Lightning strikes recorded from 06:00 UTC to 12:00 UTC on the April 11, 2012 by means of the lightningmaps.org network for lighting and thunderstorms, retrieved by the online archive. Courtesy www.lightningmaps.org.

types of squall lines, the line motion is the result of two contributions: the advection motion of individual cells which tend to move with the mean environmental wind averaged in the 0–6 km layer and the discrete propagation due to the triggering of new cells along the leading edge of the spreading gust front of the squall line.

For most squall lines, the overall speed of propagation tends to be controlled by the propagation speed of the squall line gust front. Often but not always, squall lines are oriented in mid-latitudes along the cold front (North-South) of an extratropical cyclone and they propagate Eastwards, but the storm also tends to move with different velocity from the synoptic wind in the ABL. Squall line motion can also be affected by variations in the environmental condition along the line (i.e. atmospheric instability or lower level of free convection), thereby promoting a line motion toward region with more favourable environmental conditions. These considerations led the authors to the conclusion that the distinction between storm motion and ABL wind is crucial in the development of

Table 8
Abrupt change analysis in the standard deviation for the La Spezia downburst event of April 11, 2012.

	Anemometer SP 03	Anemometer SP 02
v_b^-	7.8 m/s	5.9 m/s
α_b^-	126°	126.3°
v_{max}	18.5 m/s	23.3 m/s
α_{max}	223.8°	197°
Δt_{II}	431 s ≃ 7 min	337 s ≃ 6 min
Δt_{III}	344 s ≃ 6 min	847 s ≃ 14 min
$\Delta t_{tot} = \Delta t_{II} + \Delta t_{III}$	775 s ≃ 13 min	1184 s ≃20 min
v_b^+	4.5 m/s	3.2 m/s
α_b^+	148.4°	165.1°

Table 9
Parameters for the simulation of La Spezia Downburst, April 11, 2012.

1	$v_{r,max}$	18.8 m/s	Maximum radial velocity
2	R	505 m	Downdraft radius
3	T_1	1680 s	Period of linear intensification of the intensity-decay function (Π_r)
4	T_f	3030 s	Duration of the downburst event (Π_r)
5	x_{C_0}	3282.6 m	Initial location along the x axis of the touch-down (t = 0)
6	y_{C_0}	−6239.2 m	Initial location along the y axis of the touch-down (t = 0)
7	v_t	4.4 m/s	Downburst translation speed
8	α_t	133.6°	Downburst translation direction
9	v_b	5.35 m/s	Low – level ABL wind speed
10	α_b	141.45°	Low – level ABL wind direction

analytical methods capable of outlining ever more detailed aspects of downburst outflows wind. The study of two downburst carried out by Hjelmfelt (1988) through radar measurements clarify the importance of this issue. In one case he described a nearly stationary downburst (i.e. in

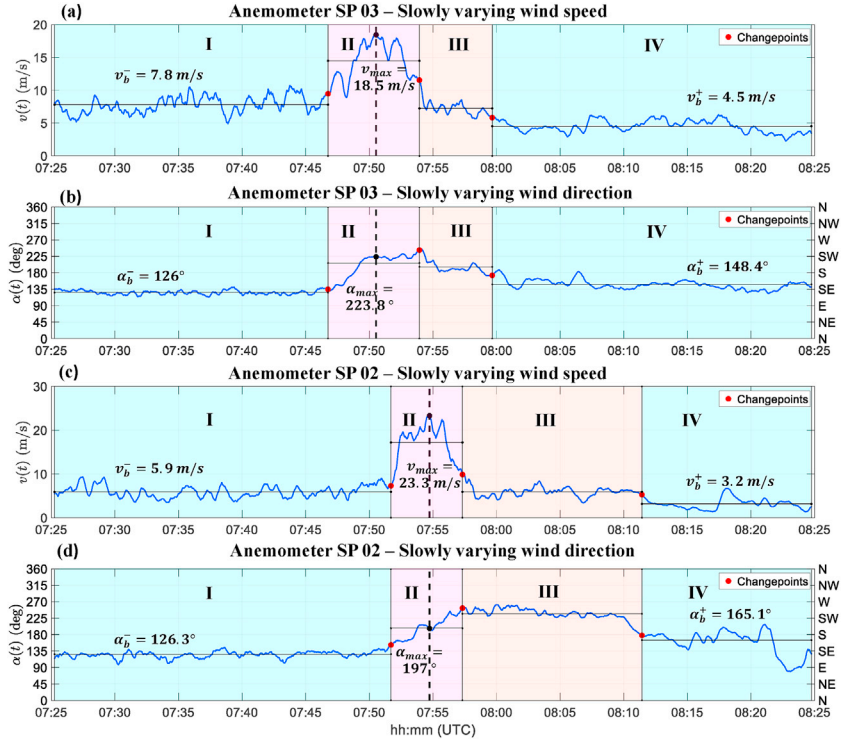

Fig. 18. La Spezia monitoring network from 07:25 UTC to 08:25 UTC on April 11, 2012. **(a), (b)** slowly varying mean wind speed v and direction α measured by the anemometer SP 03; **(c), (d)** slowly varying mean wind speed v direction α measured by the anemometer SP 02. Vertical dashed lines show approximately the passage of the downburst event.

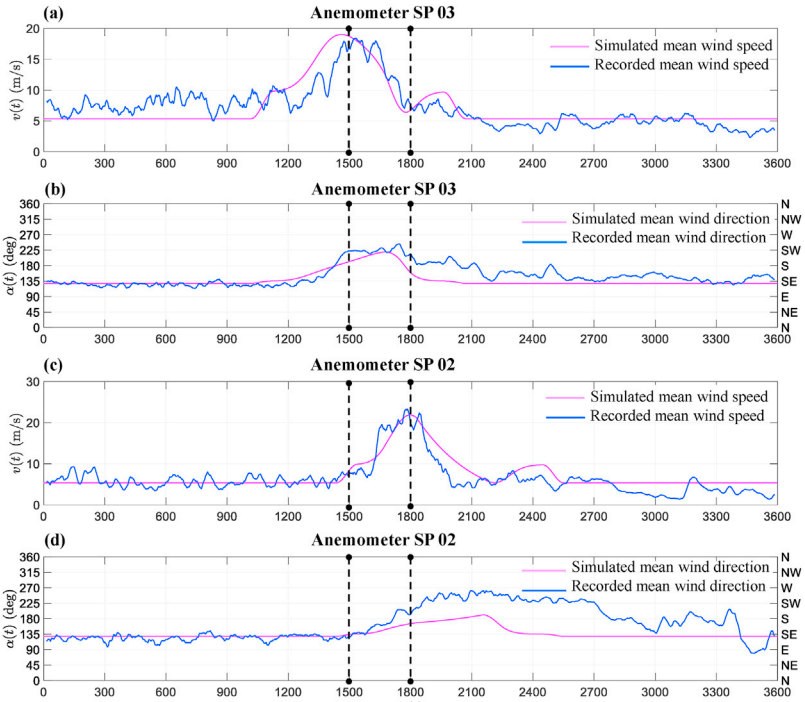

Fig. 19. Simulation of La Spezia downburst, April 11, 2012. Comparison between the simulated and recorded mean wind speed **(a)** and direction **(b)** for the anemometer SP 03 and simulated and recorded mean wind speed **(c)** and direction **(d)** for the anemometer SP 02.

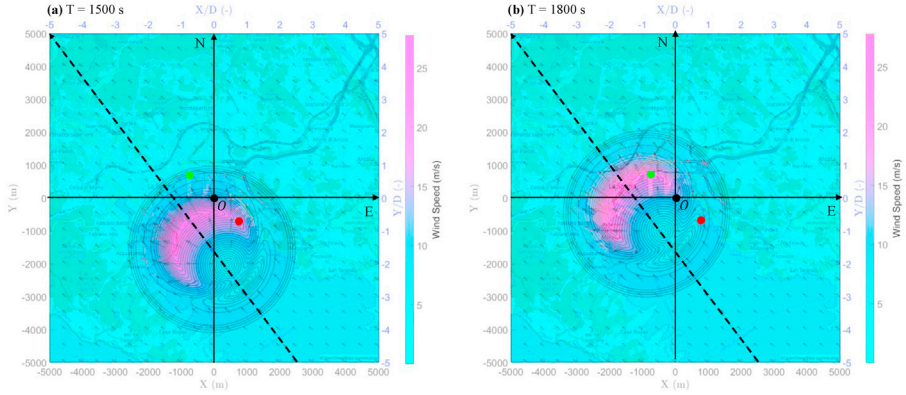

Fig. 20. Simulation of Genoa Downburst, September 30, 2012. **(a)** simulation time = 1500 s; **(b)** simulation time = 1800 s. The red dot indicates the position of the anemometer SP 03; the green dot indicates the position of the anemometer SP 02. The black dot indicates the origin *O* of the reference frame and is the geometric centre of the two anemometers. The black dashed line indicates the downburst path.

the absence of storm motion, or very weak motion) embedded in strong low-level environmental winds; in the second case he described a counterpart example in which a fast translating downburst occurred in an environment with very low or absence of ABL flow. Without an explicit distinction between the ABL flow and the storm motion, any analytical model would not be able to describe these two real cases.

Starting from these premises, this paper proposes an analytical model that reconstructs the horizontal mean wind velocity at a fixed height above the ground, originating from a travelling downburst. The combined wind velocity experienced at a point where a downburst passes, is assumed to be the vector summation of three independent velocity fields, namely the radial impinging jet velocity due to a stationary downburst, the translation velocity of the storm cell and the low-level ABL wind velocity where the downburst winds near the surface are embedded (Burlando, 2019). It is worth noting that the storm motion induces downdraft translation/advection with respect to the ground, while the downburst wind, near the surface, can be perturbed by the presence of the low-level environmental winds.

Accordingly, the motivation for the development of this model is twofold:

- To reconstruct anemometer records produced by downburst in the Northern Mediterranean Sea and to determine the physical structure and dimensions of these events.
- To make a preliminary step forward towards the development of a new wind loading model of downburst for design of structures.

With regards to these two points, the model employs only parameters that are related to meteorological variables and are susceptible for a statistical assessment (Ponte and Riera, 2007; Aboshosha et al., 2017), including the correlation between different quantities. It is worth noting however that before conducting statistical analyses a considerable meteorological research is required.

A parametric analysis is also developed here and coupled with the

analytical model in order to investigate two observed downburst events. This aim is achieved by means of an optimization procedure which allows to determine the parameters of the model and hence to reconstruct the space-time evolution of downbursts.

Furthermore, for each event considered in this paper, a meteorological analysis has been performed, in order to investigate their physical nature. This analysis was mainly performed by means of satellite images, composite radar imagery, and lighting activity. The meteorological analysis of the events considered here may be helpful for clarifying the relation between the shape of the anemometric signals, investigated for instance by Burlando et al. (2018), and the underlying meteorological phenomena.

The paper is organized into six Sections. After these introductory notes, Section 2 describes the full-scale measurements dataset used in the current study. Section 3 illustrates the implementation of the new analytical model for simulating thunderstorm outflows. Section 4 provides a parametric study which is coupled with the analytical model in order to determine the parameters on which the model depends and therefore to reconstruct the space-time evolution of the thunderstorm full-scale events considered in this paper; these parameters represent key features for evaluating the wind loading of structures. Section 5 introduces a synthetic meteorological survey coherent with the methodology described by Burlando et al. (2018) and the space-time reconstruction of two thunderstorm downburst full-scale events. While one event is recorded by one anemometer in the Port of Genoa, the second event is recorded by two anemometers located at different position in the Port of La Spezia. In the latter case the reconstruction analysis is performed in order to reconstruct the time and space evolution of the downburst event as seen by the two anemometers. Section 6 summarizes the main conclusions and provides the many prospects opened by this research.

2. Full scale measurements

The full-scale dataset used in this paper derives from the two European Projects “Wind and Ports” (WP, 2009–2011) (Solari et al., 2012) and “Wind, Ports and Sea” (WPS, 2013–2015) (Repetto et al., 2017, 2018). Carried out by the Department of Civil, Chemical and Environmental Engineering (DICCA) of the University of Genova in collaboration with the port authorities of Genoa, Savona, La Spezia, Livorno and Bastia, the main goal of these projects was to establish an extensive monitoring network in the northern Mediterranean Sea, with the purpose of collecting data for short- and medium-range wind forecasting as well as to create a statistical database of different wind conditions in the Tyrrhenian Sea. A total of 28 bi-axial and three-axial ultrasonic anemometers were installed throughout the ports. The anemometer sampling rate is 10 Hz (except for the anemometers in Bastia which have a sampling rate of 2 Hz) and their precision is 0.01 m/s for wind speed and 1° for wind direction. Depending on the port, the anemometer height varies from 10 to 75 m Above the Ground Level (AGL). In addition, the monitoring network now includes three weather stations and three LiDAR wind-profilers situated in Savona, Genoa and Livorno and one LiDAR-scanner (Windcube 400S) installed in the port of Genoa. A brief description of the measurements collected so far is provided in Zhang et al. (2018, 2019).

The measurements are transmitted to local servers located in each port from where 10-min statistical averages and raw data are further transferred to a central server situated in DICCA for data validation, processing and storage. Lastly, deploying a semi-automated separation procedure described in De Gaetano et al. (2014), the wind records are separated into three classes: (1) thunderstorms, (2) extra-tropical cyclones, and (3) intermediate events. As a result, over 250 strongly non-stationary thunderstorm records are available from the monitoring system (Zhang et al., 2018).

For the present analysis, two thunderstorm downburst events detected by anemometers in the Port of Genoa and La Spezia in the period from April to September 2012 are considered. While the downburst event in the Port of Genoa was measured by one anemometer, the second event in the Port of La Spezia was registered by two anemometers, therefore the total number of analyzed downburst records is three. Fig. 3 shows the location of these anemometers while Table 1 reports the main characteristics of the downburst records analyzed in this paper; they include the instantaneous peak wind velocity, v_{max}, the maximum value of the slowly-varying mean wind velocity, $\bar{v}_{max}$, and the wind direction α at the time of v_{max}.

It is worth noting that the strongest event analyzed in this study was recorded in La Spezia with $v_{max} = 32$ m/s at 10 m AGL. Besides, examining α together with Fig. 1, it is clear that all the examined downbursts were spawned above sea and moved towards the shore. The same patterns have been observed for most of the other events, namely, downbursts are typically generated above sea and afterward advance inland (Burlando et al., 2017).

The individual anemometer records of the horizontal wind velocity and direction are decomposed into a slowly varying running mean and a residual turbulent fluctuation. Since the turbulent fluctuation is not included in this study, only the slowly varying running mean of the wind velocity and direction are considered.

A number of techniques have been used to derive the time-varying mean for non-stationary thunderstorm winds. They include the moving average technique, adopting a suitable time interval (Choi and Hidayat, 2002; Lombardo et al., 2014; Solari et al., 2015; Zhang et al., 2018, 2019; Junayed et al., 2019, Tubino and Solari, 2020) and a broad class of advanced procedures such as the discrete wavelet transform, empirical mode decomposition and variable averaging interval schemes (Chen and Letchford, 2005; McCullough et al., 2014; Su et al., 2015; Hung et al., 2015). These latter techniques are generally considered as more refined, although they are often based on a subjective choice of the parameters (e.g. the wavelet type and order and the number of decomposition levels to be taken into account in wavelet transform, as well as the number of lower level intrinsic mode functions to be subtracted in empirical mode decomposition). Under this point of view the moving average can be considered as the simplest and most straightforward procedure, only requiring the definition of the averaging time interval (usually around $T = 30$ s).

For this reason, the Authors of this paper chose to apply a simple technique, namely the moving average approach. Consequently, the slowly varying mean wind velocity, which from now on will be called $v(t)$, and the slowly varying mean wind direction, which will be called hereafter $\alpha(t)$ are extracted using the directional decomposition rule for thunderstorm outflows proposed by Zhang et al. (2019). Each time history record employed in the current work has a duration $\Delta t = 1$ h (Burlando et al., 2018) and is decomposed considering a moving average period $T = 30$ s (Solari et al., 2015; Zhang et al., 2019).

3. Model implementation

This section describes the implementation of an analytical model aiming to simulate the horizontal mean wind velocity and direction, evaluated at a generic point belonging to a horizontal plane with a fixed height z AGL, originating from a travelling downburst whose outflow is embedded in a low-level ABL wind. The combined wind velocity and direction experienced at that point, for instance the location of a wind sensor or a structure, is assumed to be the vector summation of three independent velocity fields, namely the radial impinging jet velocity due to a spatially-stationary but time-evolving downburst (Section 3.1), its translation velocity due to the parent-storm motion (Section 3.2) and the low-level ABL wind velocity of synoptic nature into which the downburst winds near the surface are embedded (Section 3.3).

3.1. Wind field due to a stationary downburst

In the initial modelling stage, it is assumed that the parent-storm from

which the downburst descends does not move relatively to the ground; so, a spatially stationary downburst (or non-translating downburst) is considered. From a physical point of view a necessary ingredient for this type of downburst to take place is a quiescent environment (i.e. absence or very weak ABL wind shear). When the downdraft impinges on the ground, it begins to spread with a starburst outflow generating strong diverging winds. This type of downburst with nearly radially symmetric outflows was described by Fujita (1985).

The explanation of the strong diverging wind is the result of the formation of vortex rings. A primary low-pressure vortex ring forms around the high-pressure at the downburst centre and stretches gradually with time, propagating away from the downdraft core. The superposition of the outflow and vortex fields creates a region of very high radial wind speed (Jesson and Sterling, 2018). Numerical simulations also indicate the development of a smaller, secondary vortex at the base of the primary one (Kim and Hangan, 2007; Mason et al., 2009), caused by the interaction of the flow with the surface roughness. A secondary radial velocity peak may occur as the secondary-vortex ring further develops inside the outer boundary of the downburst (Le and Caracoglia, 2017).

Fig. 4 shows a schematic representation of the downburst and the parameters that describe the outflow structure, as adapted from Hjelmfelt (1988). Here, $R = D/2$ represents the radius of the downdraft, $R_{max} = D_{max}/2$ is the radial distance from the downburst centre at which the maximum radial velocity ($v_{r,max}$) occurs, and $R_E = D_E/2$ is the radial extension of the outer edge of the outflow (or gust front) from the downburst centre. Hjelmfelt (1988) reported that, on average, the maximum outflow intensity occurs for $R_E \approx 2R_{max}$. This latter indication will be useful when modelling the storm motion. Fig. 1 provides an indication of the average value assumed by the parameters mentioned above.

In this work the horizontal mean wind velocity at a fixed height z AGL due to a stationary downburst is reconstructed starting from the Holmes and Oliver model (2000), being an empirical model based on a function that describes the radial profile of the mean horizontal wind velocity, which is calibrated by means of laboratory tests of axisymmetric impinging jet on a flat surface (Poreh and Cermak, 1959) and by the radar observations of microburst events described by Hjemfelt (1988). This model includes also an intensity function Π_r that simulates the event's decreasing intensity on increasing the time. This was modified by Chay at al. (2006) so that the model could represent the full life of the storm and therefore it can simulate also the period of intensification at the start of the event.

Considering an $x - y$ fixed Cartesian reference frame with origin in O, where x is aligned with the East direction and increases toward East and the y axis is aligned with the North direction and increases toward North (see Fig. 5). Assuming that the coordinate of the downburst downdraft centre is $C_0(x_{C0}, y_{C0})$ (i.e. the touch down position at time $t = 0$). Besides, taking a generic point $P(x_P, y_P)$ inside the domain in which the reconstruction of the horizontal wind field has to be performed. According to the Holmes and Oliver model (2000), at time t the generic point P will experience a horizontal wind speed given by the following equation:

$$v_r(r,t) = v_r(r) \cdot \Pi_r(t) \tag{1}$$

with:

$$v_r(r) = \begin{cases} v_{r,max} \cdot \left(\dfrac{r}{R_{max}}\right), 0 \le r \le R_{max} \\ v_{r,max} \cdot exp\left[-\left(\dfrac{r - R_{max}}{R_s}\right)^2\right], \; r > R_{max} \end{cases} \tag{2}$$

According to this model, in the stagnation region, defined as the region where $0 \le r \le R_{max}$, r being the radial distance between the downburst centre and the observation point P, the horizontal radial velocity increases linearly on increasing the radial distance from the stagnation point ($r = 0$), up to the radial distance R_{max} where the maximum velocity occurs, whereas, in the decay region, an exponential decay of the horizontal radial velocity occurs. R_s is a radial length scale of the downburst and is schematically indicated in Fig. 5. According to Holmes and Oliver (2000) there is a good agreement between the radial profile of the horizontal wind velocity described by Eq. (2) and the radar observation described by Hjelmfelt (1988) when $R_s = 0.5 \cdot R_{max}$. The position R_{max} at which the maximum radial velocity occurs can be assumed as a ratio of the downdraft width D. The value of this parameter implemented in the new model, $R_{max} = 1.0 \cdot D$, is in good agreement with the values reported in literature (Chay et al., 2006, Kim and Hangan (2007) and Xu et al. (2008)).

This choice implies that $R_s = R$, so it is possible to give a physical interpretation to the radial length scale which in the new model coincides with the downdraft radius.

Π_r is a function that takes into account the time dependency of the storm intensity. According to the model proposed by Chay et al. (2006), it is referred to as the intensity-decay function and is given by the following relationship:

$$\Pi_r(t) = \begin{cases} \dfrac{t}{T_1} \quad , \; t \le T_1 \\ exp\left[-\dfrac{(t - T_1)}{c}\right], \; t > T_1 \end{cases} \tag{3}$$

where T_1 is the period of the linear intensification from the starting instant to the maximum outflow speed; c is an exponential decay time constant. Considering that this phenomenon dissipates at the time T_f, which is assumed to correspond to $\Pi_r(T_f) = 0.1$, it is possible to link the value of c with the period that represents the decay phase of the phenomenon:

$$c = \frac{T_f - T_1}{\ln(10)} \tag{4}$$

Assuming that the period of the downburst decay has a lower bound of 5 min and an upper bound of 35 min, then typical values of the exponential decay constant will stay in the range $2.2 \le c \le 15.2$ min. It is worth noting that the intensification period of the downburst and the downburst age cannot directly be evaluated from the observed downburst time series. The event may either be born and spend parts of its life before the observation points since it or the observation points could record all the life cycle if it is born and ends inside their observation range. For the reconstruction of the entire horizontal wind field due to a spatially stationary downburst it is convenient to express the horizontal wind speed vector in terms of its Cartesian components:

$$\begin{cases} v_x^{(r)}(x_P, y_P, t) = v_r(r) \cdot \Pi_r(t) \cdot cos(\beta_r) \\ v_y^{(r)}(x_P, y_P, t) = v_r(r) \cdot \Pi_r(t) \cdot sin(\beta_r) \end{cases} \tag{5}$$

where $v_x^{(r)}$ is the zonal velocity, i.e. the component of the horizontal wind speed towards East, and $v_y^{(r)}$ is the meridional velocity, i.e. the component of the horizontal wind speed towards North, where $r = \sqrt{(x_P - x_{C0})^2 + (y_P - x_{C0})^2}$ and $\beta_r = atan2[(y_P - y_{C0})/(x_P - x_{C0})]$, with $atan2$ the four-quadrant inverse tangent. Accordingly, β_r is a wind vector polar angle that represents the radial direction from the downburst centre to the observation point $P(x_P, y_P)$; it increases anticlockwise from the positive x-axis, i.e. from East (Fig. 5).

3.2. Storm motion - translating downburst

In the second modelling stage, the parent cloud producing the downburst is assumed to be in movement. Because of this motion, the front side of the storm intensifies while the back-side weakens, resulting in a strongly diverging directional flow (Fujita, 1985).

Downburst outflows can be produced in almost all types of convective

storms. These types of storm are standardly categorized as single-cell storm, multi-cell and supercell storm.

Observations indicate that the environmental wind in which the storm is embedded, in particular the vertical wind shear (i.e. the change of the horizontal wind speed and direction with the height), plays an important role in the motion of isolated convective storms. In the early studies about the movement of the convective cells detected by a radar, Brooks (1946) observed that small cells (mostly about 5 km in diameter) tend to move with the environmental wind in the lower part of the cloud layer. Byers and Braham (1949) found that small radar echoes observed during the Thunderstorm Project generally moved with the mean environmental wind in the cloud layer up to 6 km AGL. The mean environmental wind is evaluated as an integral measure of the horizontal wind velocity variation between 0 and 6 km AGL. Brooks (1946) also noted that when multicellular storms are present in an environment with significant vertical shear, new cells tend to form on a preferred flank of the storm. Thus, he introduced the concept that the movement of a group of cells differs from that of the individual cells, owing to the effect of discrete propagation. As a consequence, what we usually call storm motion is actually the sum of two contributions: advection or continuous propagation of individual cells (i.e. cell motion) and discrete propagation due to the generation of new cells in a preferred flank of the storm (Marwitz, 1972). Other observations of convective storms indicate that the vertical wind shear increases from single-cells to multi-cells and even more to supercells (Chisholm and Renick, 1972) as shown in Fig. 6.

What emerges from these studies is that the storm motion has a propagation speed and direction which is different from the low-level environmental winds, i.e. the background wind found in the ABL, whose height is in the order of 1 km AGL. Thus, these winds occur under the parent cloud base. The analytical models currently present in literature to describe a translating downburst do not make a clear and precise separation between the storm movement and the winds in the ABL. In fact, in the first analytical model of a travelling downburst presented by Holmes and Oliver (2000), as well as in most of the following models, it seems that the storm motion coincides with the low-level ABL wind. The Authors claim, instead, that the distinction between the storm motion and the ABL wind may be crucial. In particular, the storm motion causes the translation of the downburst while the downburst wind near the surface is perturbed by the presence of the low-level ABL winds. Accordingly, the present model assumes a clear distinction between the translational velocity of the downburst cell, $\vec{v}_t$ and the ABL wind $\vec{v}_b$.

More precisely, it is assumed that the translating downburst moves with a constant velocity $\vec{v}_t$ along the downburst path, which is conventionally defined as a straight line and identified by the trajectory of the downburst centre. Thus, the equation of the downburst motion in Cartesian coordinates is given by:

$$\begin{cases} x_C(t) = x_{C0} + v_t \cdot t \cdot cos(\beta_t) \\ y_C(t) = y_{C0} + v_t \cdot t \cdot sin(\beta_t) \end{cases} \tag{6}$$

where β_t is the polar angle that identifies the translational direction of the downburst, i.e. the angle measured anticlockwise between the positive x-axis and the downburst path (Fig. 7). By conservation of horizontal momentum, when the downburst cell has a motion relative to the ground, then the cell's translational velocity has to be added to the radial outflow, with an increase in velocity relative to the surface on the leading edge and a decrease in velocity on the trailing edge.

As far as the translating downburst velocity is concerned, it is applied only to a limited circular area with diameter D_E around the downburst, while it is zero outside this area. This paper assumes that this circular area coincides with the outer edge of the outflow (outflow front) at its maximum intensity, as described by Hjelmfelt (1988), thus $D_E = 2 \cdot D_{max}$ (see Fig. 4). So D_E, like the parameter R_{max}, is kept fixed in this model. In order to apply the translation velocity to the circular area of the outflow front, an auxiliary function of space and time Δ has to be introduced with the following characteristics:

$$\Delta(r,t) = \begin{cases} 1 \quad , 0 \le r(t) \le R_E \\ \frac{1}{2} \cdot \left\{ 1 + cos\left[\frac{\pi}{a \cdot R_E} \cdot (r(t) - R_E) \right] \right\}, \; R_E < r(t) \le R_{E,max} \\ 0 \quad , r(t) \ge R_{E,max} \end{cases} \tag{7}$$

The auxiliary function Δ is shown in Fig. 7, it is positioned at the centre of the downburst and moves along the downburst path. The various parameters that appear in Eq. (7) are described below:

$r(t) = \sqrt{(x_P - x_c(t))^2 + (y_P - y_c(t))^2}$ is the relative distance between the downburst centre and the observing point P, since the storm moves, this distance changes with time.

$R_E = 2 \cdot R_{max} = 4 \cdot R$, as said above, is a fixed model parameter and is identified with the radial extension of the outer edge of the outflow from the downburst centre.

$R_{E,max} = (1 + a) \cdot R_E$ is a fixed model parameter. In order to be consistent with the Hjelmfelt (1988) observation concerning the size of the outflow outer edge and, at the same time, to guarantee a smoother transition from zero to the downburst translational velocity v_t, hence avoiding a sudden discontinuity in the model (see Fig. 7), a reasonable value of the parameter a is $a = 0.2$. Values of a less than 0.2 would create an abrupt transition from zero to v_t while a value of a greater than 0.2 would increase the size of the outflow outer edge and would not be consistent with the values observed in literature.

Fig. 7 provides a schematic representation of the translating downburst. Consequently, the vector field due to the translational velocity in Cartesian coordinates (zonal and meridional velocity) is given by the vector summation of the radial outflow and the translation velocity of the downburst cell:

$$\begin{cases} v_x(x_P, y_P, t) = v_x^{(r)}(x_P, y_P, t) + v_x^{(t)}(x_P, y_P, t) \\ v_y(x_P, y_P, t) = v_y^{(r)}(x_P, y_P, t) + v_y^{(t)}(x_P, y_P, t) \end{cases} \tag{8}$$

Expanding Eq. (8) leads to:

$$\begin{cases} v_x(x_P, y_P, t) = v_r(r) \cdot \Pi_r(t) \cdot cos(\beta_r) + v_t \cdot cos(\beta_t) \cdot \Delta(r,t) \cdot \Pi_t(t) \\ v_y(x_P, y_P, t) = v_r(r) \cdot \Pi_r(t) \cdot sin(\beta_r) + v_t \cdot sin(\beta_t) \cdot \Delta(r,t) \cdot \Pi_t(t) \end{cases} \tag{9}$$

In Eq. (9), besides the intensity-decay function Π_r applied to the radial component of the downburst, a new intensity-decay function Π_t is introduced and is applied to the translational component of the downburst. Π_t is provided by the relationship:

$$\Pi_t(t) = \begin{cases} \frac{1}{2} \cdot \left\{ 1 + cos\left[\frac{\pi}{T_i} \cdot (t - T_i) \right] \right\}, \; 0 \le t \le T_i \\ 1 \quad , T_i < t \le T_f \\ \frac{1}{2} \cdot \left\{ 1 + cos\left[\frac{\pi}{b \cdot T_f} \cdot (t - T_f) \right] \right\}, \; T_f < t \le T_{f,max} \\ 0 \quad , t > T_{f,max} \end{cases} \tag{10}$$

The parameters that appear in Eq. (10) are all fixed model parameters and are related to the parameter that describes the intensity-decay function of the radial velocity field, Π_r. So, their values are $T_i = b \cdot T_1$ and $T_{f,max} = (1 + b) \cdot T_f$ with $b = 0.2$, where T_1 is the linear intensification period of the function Π_r while $T_f = T_1 + c \cdot \ln(10)$ is the period in which $\Pi_r(T_f) = 0.1$. The graph of the intensity-decay function of the radial and translational component of the downburst are given respectively in Fig. 8a and b.

Regarding the function Π_t, the values that it assumes in the intervals $0 \le t \le T_i$ and $T_f < t \le T_{f,max}$ are introduced in order to avoid jump discontinuities in the model, whereas the unitary value that Π_t assumes in the interval $T_i < t \le T_f$ is introduced to ensure a constant translational velocity of the downburst cell.

3.3. Translating downburst embedded in a low-level ABL wind

In the third and final modelling stage it is assumed that the downburst cell translates in an environment which is characterized by the presence of a low-level ABL wind, usually of synoptic type, characterized by different wind speed and direction compared to the downburst cell motion. So, beside the storm motion, the wind field near the surface due to a translating downburst can be significantly disturbed by the surface ABL wind. The latter is considered constant in speed and direction in the whole domain under consideration and is given by:

$$\begin{cases} v_x^{(b)} = v_b \cdot cos(\beta_b) \\ v_y^{(b)} = v_b \cdot sin(\beta_b) \end{cases} \tag{11}$$

where v_b is the mean ABL wind velocity (at height z AGL), which forms the angle β_b with the positive x-axis. It is also assumed that the resulting velocity vector, at the generic point P, may be obtained as the vector summation of the wind fields due to the translating downburst and the low-level environmental wind velocity. Then, referring to Eqs. (9) and (11), the resultant velocity components are given by:

$$\begin{cases} v_x(x_P, y_P, t) = v_x^{(r)}(x_P, y_P, t) + v_x^{(t)}(x_P, y_P, t) + v_x^{(b)} \\ v_y(x_P, y_P, t) = v_y^{(r)}(x_P, y_P, t) + v_y^{(t)}(x_P, y_P, t) + v_y^{(b)} \end{cases} \tag{12}$$

Expanding Eq. (12) one obtains:

$$\begin{cases} v_x(x_P, y_P, t) = v_r(r) \cdot \Pi_r(t) \cdot \cos(\beta_r) + v_t \cdot \cos(\beta_t) \cdot \Delta(r,t) \cdot \Pi_t(t) + v_b \cdot cos(\beta_b) \\ v_y(x_P, y_P, t) = v_r(r) \cdot \Pi_r(t) \cdot sin(\beta_r) + v_t \cdot sin(\beta_t) \cdot \Delta(r,t) \cdot \Pi_t(t) + v_b \cdot sin(\beta_b) \end{cases} \tag{13}$$

According to Eq. (13) the module and the direction of the horizontal wind vector at the point $P(x_P, y_P)$ are given by the relationships:

$$v(x_P, y_P, t) = \sqrt{v_x(x_P, y_P, t)^2 + v_y(x_P, y_P, t)^2} \tag{14}$$

$$\beta(x_P, y_P, t) = atan2\left(\frac{v_y(x_P, y_P, t)}{v_x(x_P, y_P, t)}\right) \tag{15}$$

Finally, instead of using the polar angle β, the model uses the meteorological wind direction, i.e. the direction from which the wind is blowing. The former is called herein α and increases clockwise from the positive y-axis (i.e. from the North). The relation between α and β is straightforward and is given by:

$$\alpha(x_P, y_P, t) = 270^\circ - \beta(x_P, y_P, t) \tag{16}$$

The advantages of the above reconstruction are multiple. Each point in the domain may be treated as a surface station that records the wind speed and direction of a travelling downburst embedded in the low-level ABL flow. This allows to simulate a single event which is recorded by several stations. Also, the model is able to distinguish between different cases that may occur in nature, for example, a stationary downburst (i.e. absence of storm motion, or very weak motion) embedded in a strong low-level ABL wind or a fast translating downburst with very low or absence of ABL wind.

It is worth noting, however, the preliminary character of the proposed model and the necessity of clarifying the reliability of some assumptions at its base. The most relevant issue concerns the vector combination of the stationary downburst velocity, the translational velocity of the thunderstorm cell and the low-level ABL wind velocity. While using a vector combination of the stationary downburst velocity and the translational velocity of the thunderstorm cell seems to be appropriate, the further vector combination with the low-level ABL wind velocity is highly questionable as pointed out by some preliminary wind tunnel experiments (Romanic and Hangan, 2018). In this regard, systematic laboratory tests have been recently conducted in the framework of the THUNDERR project (Solari et al., 2020) and the results are under process. This aspect will be further discussed in the prospects.

The analytical model described above has been implemented in MATLAB. Table 2 summarizes the parameters on which it depends. They are necessary for the reconstruction of the thunderstorm event considered and consequently vary from case to case. Table 3 summarizes the fixed model parameters used in the paper; they are the same for all the study cases herein considered. In perspective, all these parameters may be transformed into free parameters to be evaluated case by case. In particular some fixed parameters such as R_{max} or R_E could be better calibrated in future works starting from experimental and numerical studies (CFD) of downburst events. It is worth mentioning, however, that in the literature other value of the radial position of the maximum radial velocity are suggested. Using full-scale measurements Hjelmfelt (1988) proposed $R_{max} = 0.75 \cdot D$ to $1.0 \cdot D$, while Mason et al. (2009) found $R_{max} = 1.25 \cdot D$ based on numerical simulations.

4. Parametric analysis

In this section a parametric analysis is undertaken on the parameters of the analytical model. The purpose of the study is the creation of a wide set of events to compare with observations in order to get the actual downburst's dimensions and relevant kinematic parameters of specific test cases according to a minimization function between simulation and measurements. The different field parameters that describe the downburst outflows such as the downdraft radius, linear intensification period, total duration of the event, touch-down position, downburst translational velocity and direction are estimated by relating the recorded downburst data to the parametric analysis.

As far as the evaluation of the wind speed and direction of the low-level ABL wind is concerned, it is determined using a signal processing technique that detects abrupt changes in the standard deviation of downburst velocity signals. This technique, previously applied in signal processing evaluations concerning speech recognition, brain research (Lavielle, 2005) and geoscience (Killick et al., 2012), has been successfully applied for the first time to a real downburst case by Romanic et al. (2019a) in order to objectively detect the moments of abrupt changes in the wind speed downburst time series. This method accurately identifies the surface ABL wind before and after the passage of the downburst outflow; it is also capable of objectively determining the duration of the downburst event.

Before introducing the implementation of the parametric analysis in Section 4.2, a brief description of the abrupt change technique is given in Section 4.1.

4.1. Abrupt change technique for determining the low-level ABL wind

An abrupt change or changepoint is a sample or time instant at which some statistical property of a signal changes abruptly. The statistical property in question can be the mean of the signal, its standard deviation or spectral characteristics among others. The signal processing technique is applied in the current work only to the slowly varying wind speed v and the statistical property considered here is the standard deviation.

However, in order to explain the procedure let us start from applying this algorithm to the mean as follows: given the time series $v_1, v_2, \ldots, v_N$, where N is the total number of recorded samples, let us seek to determine a signal changepoint, k, by minimizing the total residual error of the cost function J:

$$J(k) = \sum_{i=1}^{k-1} \left(v_i - \overline{v}_{1,k-1}\right)^2 + \sum_{i=k}^{N} \left(v_i - \overline{v}_{k,N}\right)^2, \; k = 1, 2, \ldots, N \tag{17}$$

Namely, the cost function J chooses a point k and divides the signal into two sections and then the mean is calculated for each section, i.e. $\overline{v}_{1,k-1}$ and $\overline{v}_{k,N}$. Then, for every point v_i within a section the deviation of the mean from that point is calculated and then the deviation from all the points is added. Afterward, the deviations for all the points are added

segment to segment in order to find the value of the function $J(k)$. Finally, the location of the division point k is varied, i.e. $k = 1, 2, \ldots N$, until the cost function $J(k)$ attains a minimum, namely a changepoint K is the one for which $J(K) = min\{J(k)\}_{k=1}^{N}$. Expanding Eq. (17) it follows that:

$$J(k) = \sum_{i=1}^{k-1}\left(v_i - \frac{1}{k-1}\sum_{r=1}^{k-1} v_r\right)^2 + \sum_{i=k}^{N}\left(v_i - \frac{1}{N-k+1}\sum_{r=k}^{N} v_r\right)^2, k = 1, 2, \ldots, N \tag{18}$$

Eq. (18) can also be expressed by using the definition of variance (Var), namely:

$$J(k) = (k-1)\cdot Var([v_1,\ v_2, \ldots, v_{k-1}]) + (N-k+1)\cdot Var([v_k,\ v_{k+1}, \ldots, v_N]) \tag{19}$$

Eq. (19) can be generalized to incorporate other statistics and its general form reads:

$$J(k) = \sum_{i=1}^{k-1}\Delta(v_i; \chi([v_1,\ v_2, \ldots, v_{k-1}])) + \sum_{i=k}^{N}\Delta(v_i; \chi([v_k,\ v_{k+1}, \ldots, v_N])),\ k = 1, 2, \ldots, N \tag{20}$$

where χ is the given section empirical estimate and Δ is the deviation measure. Since in this work abrupt changes in the signal are identified by considering as a metric the standard deviation, Eq. (19) can be re-written in terms of standard deviation (for details refer to Romanic et al., 2019a and Romanic et al., 2020):

$$\begin{aligned} J(k) &= (k-1)\cdot \ln\{Var([v_1,\ v_2, \ldots, v_{k-1}])\} + \\ &(N-k+1)\cdot \ln\{Var([v_k,\ v_{k+1}, \ldots, v_N])\},\ k = 1, 2, \ldots, N \end{aligned} \tag{21}$$

Signals of interest have more than one changepoint. If there are M changepoints to be found in the record, they are evaluated by minimizing the penalized form of Eq. (20) (Romanic et al., 2019a):

$$J(M) = \sum_{r=0}^{M-1}\sum_{i=k_r}^{k_{r+1}-1}\Delta(v_i; \chi([v_{k_r}, \ldots, v_{k_{r+1}-1}])) + \beta\cdot M \tag{22}$$

where k_0 and k_M are respectively the first and the last sample of the signal and β is a fixed penalty constant added for each changepoint. The value of β is increased gradually until the cost function J finds M changepoints. The algorithm that minimizes Eq. (22) is based on dynamic programming with early abandonment with the details described in Lavielle (2005). Since the aim of this procedure is to identify abrupt changes in the standard deviation separating downburst winds from surface ABL flow, the number of changepoints was kept fixed and equal to $M = 3$. Once the changepoints are determined from the slowly varying mean wind speed v, then the time series is segmented into four parts and for each part the segment mean is calculated. This allows to evaluate the low-level ABL wind speed prior and after the downburst or gust front passage. Finally, the same changepoints are applied to the slowly varying mean wind direction α and, as before, the low-level ABL mean wind direction is evaluated before and after the downburst event.

4.2. Parametric analysis implementation

Table 2 provides a summary and a description of the parameters on which the analytical model established in the previous sections is built, namely ($v_{r,max}$, R, T_1, T_f, x_{C0}, y_{C0}, v_t and α_t). As far as concerns v_b and α_b, they are determined before launching the parametric analysis using the abrupt change technique introduced in Section 4.1; this leads to a reduction in the number of parameters involved in the parametric study. The object of this analysis is to estimate the most appropriate value for these eight unknown parameters, which corresponds to minimize the Normalized Mean Squared Error ($NMSE$) between the simulated and the observed slowly varying mean wind speed v and direction α. The $NMSE$ should equal 0 in case of an exact match between the simulated and recorded wind speed and directions.

A similar procedure was proposed by Abd Elaal et al. (2013b). The $NMSE$ is used here for combining the wind speed error and the wind direction error. A common choice for normalization consists on using the mean or the quadratic mean of the measured data (Bendat and Piersol, 2010): in this work the $NMSE$ is normalized by the quadratic mean of the measured data (i.e. recorded wind speed and direction). The $NMSE$ is evaluated considering a simulation time $\Delta t = 1$ h and is given by:

$$NMSE = NMSE(v) + NMSE(\alpha) \tag{23}$$

where $NMSE(v)$ is the normalized mean square difference between the computed magnitude of the simulated wind speed $v_t(v_{r,max},\ R,\ T_1, T_f,\ x_{C0}, y_{C0},\ v_t, \alpha_t)$ at time t and the magnitude of the recorded wind speed v_{Rt} at time t. The error is normalized by the mean squared value associated to the recorded wind speed v_{Rt}. So, $NMSE(v)$ is given by:

$$NMSE(v) = \frac{\frac{1}{\Delta t}\cdot\sum_{t=0}^{\Delta t}\left[v_t\left(v_{r,max},\ R,\ T_1, T_f,\ x_{C0}, y_{C0},\ v_t, \alpha_t\right) - v_{Rt}\right]^2}{\frac{1}{\Delta t}\cdot\sum_{t=0}^{\Delta t} {v_{Rt}}^2} \tag{24}$$

$NMSE(\alpha)$ is the normalized average square difference between the computed magnitude of the simulated wind direction $\alpha_t(v_{r,max},\ R,\ T_1, T_f,\ x_{C0}, y_{C0},\ v_t, \alpha_t)$ at time t and the magnitude of the recorded wind direction α_{Rt} at time t. The error is normalized by the mean squared value associated to the recorded wind direction α_{Rt}. So, $NMSE(\alpha)$ is given by:

$$NMSE(\alpha) = \frac{\frac{1}{\Delta t}\cdot\sum_{t=0}^{\Delta t}\left[\alpha_t\left(v_{r,max},\ R,\ T_1, T_f,\ x_{C0}, y_{C0},\ v_t, \alpha_t\right) - \alpha_{Rt}\right]^2}{\frac{1}{\Delta t}\cdot\sum_{t=0}^{\Delta t} {\alpha_{Rt}}^2} \tag{25}$$

Considering now the case, in which only one anemometer records the downburst event, then the anemometer is placed in the origin O of the reference $x-y$ axes. Generalization of this procedure for two or more anemometers that record the same event is given at the end of the section.

The different field parameters ($v_{r,max}$, R, T_1, T_f, x_{C_0}, y_{C_0}, α_t and v_t) and v_t) are described to be as coherent as possible with the observed data reported in literature. In this framework, the parametric analysis for each event under consideration is performed in two phases. Phase (I) has as objective to locate the sector in which the touchdown of the phenomenon occurs, whereas, Phase (II), once the sector of the touchdown position of the downburst has been identified, has the aim of carrying out a more refined analysis starting from the neighbourhood of the parameters identified in Phase (I). In this context, starting from Phase (I), in order to identify the sector from which the downburst is approaching the station, it is convenient to divide the entire simulation domain in 16 sectors as shown in Fig. 9. Let be $\psi^{(i)} = i\cdot\Delta\psi$ the angle measured clockwise from the North that describes the sectorial division of the domain, where $\Delta\psi = 22.5^\circ$ and $i = 0, 1, \ldots, 15$. The sectorial division of the domain allows to express the touchdown position, x_{C_0} and y_{C_0} in polar coordinates using $R_{C_0} = \sqrt{{x_{C_0}}^2 + {y_{C_0}}^2}$ and $\vartheta_{C_0} = atan2(x_{C_0}/y_{C_0})$ (see Fig. 9).

In Phase (I), the maximum radial velocity $v_{r,max}$ has been applied in

the range from $v_{r,max}(I) = 10$ m/s to $v_{r,max}(I) = 34$ m/s with a step increase $\Delta v_{r,max}(I)$. The downdraft radius R has been applied in the range from $R(I) = 100$ m to $R(I) = 1000$ m with a step increase $\Delta R(I)$. Therefore, the radius at which the maximum radial velocity occurs, $R_{max} = 2 \cdot R$, ranges from 200 m up to 2000 m, which is coherent with the definition of microburst given by Fujita (1985). As far as concerns the linear intensification period T_1 and the total duration of the downburst event T_f, they have been applied in the following manner: T_1 has been applied in the range from $T_1(I) = 5$ min up to $T_1(I) = 25$ min with a step increase $\Delta T_1(I)$; T_f has been applied in the range from $T_f(I) = 10$ min up to $T_f(I) = 55$ min with a step increase $\Delta T_f(I)$ and with the constrain $T_1(I) < T_f(I)$ (see Fig. 8a). Some values used for $T_1(I)$ and $T_f(I)$ are fully coherent with the radar observations given by Wilson et al. (1984) and Hjelmfelt (1988), however the scope of this analysis was also to investigate values that go beyond those reported in the literature.

The touchdown distance from the anemometer R_{C_0} has been applied in the range from $R_{C_0}(I) = 500$ m up to $R_{C_0}(I) = 8000$ m with a step increase $\Delta R_{C_0}(I)$. Assuming that the touchdown is located in the i-th sector as shown in Fig. 10, then the range of variation of $\vartheta_{C_0}^{(i)}(I)$ goes from $\psi^{(i-1)} = (i-1) \cdot \Delta\psi$ up to $\psi^{(i)} - \Delta\psi/3 = i \cdot \Delta\psi - \Delta\psi/3$ with a step increase $\Delta\vartheta_{C0}(I)$ and $i = 1, 2, \ldots, 16$. Considering now the downburst path from the i-th sector $\alpha_t^{(i)}$ (see Fig. 10), it ranges from $\vartheta_{C_0}^{(i)}(I) - \Delta\varphi/2$ up to $\vartheta_{C_0}^{(i)} + \Delta\varphi/2$ with a step increase $\Delta\alpha_t(I)$, where $\Delta\varphi(I) = 2 \cdot \mathrm{atan}(R_E(I)/R_{C_0}(I))$. The width of the angle $\Delta\varphi(I)$ ensures that the downburst always hits the station. Finally, the downburst translation speed v_t ranges from $v_t(I) = 4$ up to $v_t(I) = 16$ m/s with a step increase $\Delta v_t(I)$.

Table 4 summarizes the variation range of the eight parameters, the step increment Δ used and the number of values assumed by each parameter in order to calculate the total number of simulations during Phase (I).

This procedure is applied for each of the sixteen sectors. Accordingly, the total simulation number during Phase (I) is equal to $16 \cdot 338688 = 5419008$. All calculations were performed in MATLAB R2019a (serial computing) on a 64-bit Windows 10 Home Edition with Intel i7 (7th Gen) central processing unit (4 cores) at 3.20 GHz and 16 GB of RAM. The computing time for each simulation is about 0.1 s and consequently the total simulation time for Phase (I) is about 6 days. For each simulation, the value assumed by the eight parameters and the corresponding *NMSE* value for each of the 16 sectors was stored in a table. Consequently, analysing the table it is possible to identify the sector in which the *NMSE* attain the absolute minimum and the corresponding parameters that minimize it, this allows to identify the touchdown sector and the direction from which the downburst is approaching the station.

Let $P^*(I) = \{v_{r,max}{}^*(I),\ R^*(I),\ T_1{}^*(I), T_f{}^*(I),\ R_{C_0}{}^*(I), \vartheta_{C_0}{}^*(I),\ \alpha_t{}^*(I),\ v_t{}^*(I)\}$ be the set of parameters that minimize globally the *NMSE* in Phase (I), and let $\Delta P(I) = \{\Delta v_{r,max}(I),\ \Delta R(I),\ \Delta T_1(I), \Delta T_f(I),\ \Delta R_{C_0}(I), \Delta\vartheta_{C_0}(I),\ \Delta\alpha_t(I), \Delta v_t(I)\}$ be the set of increasing steps in Phase (I), which values are given in Table 4. The goal of Phase (II) is to refine the analysis in order to reduce further the *NMSE*, therefore let $P(II) = \{v_{r,max}(II),\ R(II),\ T_1(II), T_f(II),\ R_{C_0}(II), \vartheta_{C_0}(II),\ \alpha_t(II), v_t(II)\}$ be the parameter set in Phase (II), it's range of variation is given by the following equation:

$$P(II) = P^*(I) - \frac{\Delta P(I)}{2} \ : \Delta P(II) \ : P^*(I) + \frac{\Delta P(I)}{2} \tag{26}$$

Eq. (26) states that the range of variation of the parameters in Phase (II) goes from $P^*(I) - \Delta P(I)/2$ up to $P^*(I) + \Delta P(I)/2$ with an increasing step $\Delta P(II)$ which has chosen here to be equal to $\Delta P(I)/5$.

Table 5 summarizes the variation range of the eight parameters, the step increment Δ used and the number of values assumed by each parameter in order to calculate the total number of simulations during Phase (II).

The total number of simulations during Phase (II) is equal to 1 679 616. The time taken by the computer to perform these simulations is about two days, considering also that Phase (I) takes about 6 days, the time taken to carry out all the simulations for one single event is approximately 8 days.

Also, during Phase (II), the value assumed by the eight parameters and the corresponding *NMSE* value was stored in a table. Analysing the table, it is possible to identify the set of parameters that minimize globally the *NMSE*. The set of this parameters is called here $P^*(II) = \{v_{r,max}{}^*(II),\ R^*(II),\ T_1{}^*(II), T_f{}^*(II),\ R_{C_0}{}^*(II), \vartheta_{C_0}{}^*(II),\ \alpha_t{}^*(II), v_t{}^*(II)\}$ and their evaluation allows a meteorological reconstruction of the main parameters that describe the thunderstorm event under analysis.

Considering now the case when two or more anemometers record the same event, the procedure is straightforward to generalize. In this case, it is important to choose the origin O of the reference frame. Considering the case of N anemometers (with $N \geq 2$) a polygon is constructed having as a vertex the N anemometers. Then the geometric centre of the polygon is the new origin O of the reference frame. Then, a characteristic length of the polygon is introduced which is equal to $L_c = A_p/P_p$, where A_p is the area and P_p is the perimeter of the polygon. Finally, the same procedure as described above is applied except for the evaluation of the angle $\Delta\varphi$, which in this case is given by:

$$\Delta\varphi = \begin{cases} 2 \cdot atan\left(\dfrac{R_E}{R_{C_0}}\right), & \dfrac{L_c}{2} < R_E \\ 2 \cdot atan\left(\dfrac{\dfrac{L_c}{2}}{R_{C_0}}\right), & \dfrac{L_c}{2} \geq R_E \end{cases} \tag{27}$$

Eq. (27) ensures that the downburst is detected by all stations. In the case in which $N = 2$ (i.e. two anemometers) L_c is equal to the distance between the stations. In the case of 2 or more anemometers the *NMSE* is evaluated considering a single objective function and is given by the following equation:

$$NMSE = \sum_{i=1}^{N} [NMSE(v)]_i + \sum_{i=1}^{N} [NMSE(\alpha)]_i \tag{28}$$

The index i denotes the i-th anemometer whereas the $[NMSE(v)]_i$ and $[NMSE(\alpha)]_i$ are evaluated by Eqs. (24) and (25).

5. Reconstruction of full-scale events

In this section, in order to validate the proposed analytical model (Section 3), two different real scale events are first briefly described from the meteorological point of view (Sections 5.1 and 5.3) and then they are reconstructed by means of the parametric analysis presented in Section 4 (Sections 5.2 and 5.4). The first event is recorded by one anemometer in Genoa on September 30, 2012 (Sections 5.1 and 5.2) and the second event is recoded by two anemometers in La Spezia on April 11, 2012 (Sections 5.3 and 5.4).

5.1. Weather analysis of the downburst event occurred in Genoa on September 30, 2012

The meteorological situation over Europe on September 30, 2012 was dominated by the presence of the extratropical Cyclone Marianne (following the naming convention used by the Institute of Meteorology of the Freie Universität Berlin, Germany) located southwest of Iceland, with a surface low minimum below 980 hPa and a trough aloft extending southward to the western Alps. Besides, the 1020 hPa high-pressure maximum associated with the Anticyclone Harald, which was situated over central Europe, determined a blocking situation (Rex, 1950). The same day at 21:00 UTC, the distribution of the cloud-top heights obtained from the cloud analysis performed by Eumetsat in the infrared channel shows the presence of a smaller cyclone in the Padan plain, as shown in Fig. 11a. The cyclone, which developed on 29 September as a secondary

cyclogenesis event in the Gulf of Genoa (Burlando et al., 2017) had moved over northern Italy. The occluded front of the low-pressure system triggered strong instability and determined a wide area of cloudiness all over north Italy.

At 20:45 UTC, a thunderstorm cell moving north-northwestward was approaching the coast of Genoa from the sea. At 21:00 UTC the convective cell with cloud top heights of more than 12,000 m above the sea level reached the mature stage. At this time the thunderstorm was over Genoa as indicated by Fig. 11b. Fig. 12 shows the reflectivity measured by the composite radar imagery at 21:00 UTC, which confirms the existence of the convective cell above Genoa. Composite radar images before and after 21:00 UTC (not shown) confirm that the movement of the thunderstorm cell was toward north-northwest.

The anemometer GE.02 (see Table 1 and Fig. 3) positioned at the height 13.3 m above the ground level in the harbour of Genoa Voltri, recorded a downburst event at about 21:00 UTC. The recorded time histories of the slowly varying mean wind speed v and direction α of the downburst event, together with the abrupt change analysis for determining the low-level ABL wind, prior and after the downburst passage are presented in Fig. 13.

The anemometer registered a peak wind speed (row data, not shown) equal to 22 m/s at 21:00 UTC which marks the passage of the downburst event. The abrupt change in the standard deviation segments the signal duration of the slowly varying mean wind speed in 4 regions (3 changepoints). The same segmentation is then applied to the slowly varying mean wind direction. The first region in the records is characterized by fairly constant wind speed and direction prior to the downburst (region I in Fig. 13). The mean wind speed in this segment is $v_b^- = 2.3$ m/s and the mean wind direction is $\alpha_b^- = 40^\circ$ which are identified with the low-level ABL wind prior to the downburst passage. The region II is the main signature of the downburst event, characterized by a sudden increase in the wind speed (ramp up) and is followed by a decrease of the wind speed (ramp down) as the anemometer is in the stagnation region of the downburst (Chay et al., 2006). Therefore, region II identifies the main peak which is characterized by $v_{max} = 17$ m/s at about 21:00 UTC and has a duration of about $\Delta t_{II} = 377\ s \simeq 6$ min. In this stage the slowly-varying wind direction shifts anticlockwise from about 350° to $\alpha_{max} = 159^\circ$. The third region (III) identifies the secondary peak (mild peak) whose duration is about $\Delta t_{III} = 579\ s \simeq 10$ min. The anemometer is in the rear flank of the downburst which continues to move away from the station; also, the mean wind direction continues to shift anticlockwise up to about 90°. Finally, at the end of the record, in the region IV, the downburst passes away from the station and the low-level environmental wind after the downburst passage returns to roughly the same values of region I. In this region the mean wind speed is $v_b^+ = 3$ m/s, whereas the mean wind direction is $\alpha_b^+ = 53^\circ$. During the passage of the downburst the wind backs about 360° and the whole event, as seen by the anemometer, last roughly $\Delta t_{tot} = 579\ s \simeq 16$ min according to the abrupt change analysis in the standard deviation. The main characteristics of the abrupt change in the standard deviation for this event are summarized in Table 6.

It is noteworthy to mention that the mean wind direction α in the low-level ABL reported in Fig. 13b, slowly backs from about 45° to roughly 350° in region I, without a relevant corresponding change in the wind speed. This is thought to be not particularly relevant for the downburst modelling because there is no evidence that it might be due to the downburst itself or to the approaching thunderstorm cloud. The possibility to change the surface ABL flow along the time is not yet implemented in the analytical model, which implicitly assumes a steady ABL mean wind speed and direction.

5.2. Reconstruction of the downburst event occurred in Genoa on September 30, 2012

The values of the model parameters have been estimated by means of the parametric analysis described in Section 4, ensuring that the values of the parameters remained representative of the reference data. The mean wind speed and direction of the low-level ABL wind, were determined according to the abrupt change analysis. For this case v_b has been assumed to be the average between the ABL wind speed before and after the passage of the downburst cell, so it's equal to $v_b = 2.65\ m/s$. The same procedure has been applied to the low-level ABL mean wind direction which results $\alpha_b = 49^\circ$. The parameters that minimize the error function, *NMSE*, between the real measurements of the Genoa downburst and the simulation are summarized in Table 7.

The downdraft radius $R = 265$ m and the radius at which the maximum radial velocity occurs $R_{max} = 2 \cdot R = 530$ m agree well with the study carried out by Romanic et al., (2019b), who reported, for the same full scale event under consideration, a downburst radius of $R = 222.5$ m and a radius of maximum outflow velocity $R_{max} = 445$ m. The results of the reconstruction analysis and the comparison with the full-scale data are shown in Fig. 14, which confirms the ability of the analytical model to match the temporal profiles of the observed mean wind speed and direction. The simulated mean wind speed matches the observed data to a very good extent with $NMSE(v) = 0.0953$. At first glance, the mean wind direction might appear not properly simulated in the very first part of the signal, due to the apparent shift between the 0° and 360°; however, after this interval, the simulated mean wind direction follows well the trend of the signal with $NMSE(\alpha) = 0.3748$. For this reconstruction the combined normalized mean square error is equal to $NMSE = 0.4701$. Fig. 15 shows the simulation of the horizontal mean wind at the height of the anemometer (i.e. 13.3 m) at two snapshots in time which are indicated by the black dashed lines in Fig. 14.

The results of this simulation and, principally, the parameters that generated it (Table 7), can provide a meteorological reconstruction of the downburst event recorded in Genoa. It is worth noting that the Genoa downburst was spawned by a thunderstorm cell which was moving toward the north-northwest direction. On the other hand, according to the reconstruction by the analytical model the downburst was shot out of the cloud toward the east-northeast direction (Fig. 15), about 90° to the right of the thunderstorm motion. A similar case was described by Fujita (1983) for the well-known case of the Andrew Downburst (Fig. 2).

5.3. Weather analysis of the downburst event occurred in La Spezia on April 11, 2012

The synoptic condition over Europe on April 11, 2012 was dominated by the presence of two extratropical cyclones. The first, Jaqueline, was situated to the east of the Scandinavian peninsula with a surface low minimum below 990 hPa. The second, Klara, had formed along the frontal system of Jaqueline at around 00:00 UTC of the same day and was situated above Germany with a surface low minimum of almost 1005 hPa. As the day progressed, the low-pressure system Klara deepened and the cold front emanating from Klara extended meridionally passing over the Alps and continuing to move toward northeast. This front during the day brought heavy precipitation particularly along the Alps in the north and northeast of Italy. The distribution of the cloud top heights at 08:00 UTC in Fig. 16 shows clearly the deep convective system developing along the cold frontal boundary of Klara. In the figure, the deep convective system appears as cone-shaped cloud masses, with cloud emanating from the apex.

The composite radar imagery shown in Fig. 17a confirms the existence of a narrow, persistent band of deep convection, a feature commonly referred to as a squall line, which in this storm is coincident with the cold front advancing toward northeast. The passage of the squall line at about 07:50 UTC in the port area of La Spezia is the main contributor responsible for the strong wind event described in this section. The existence of strong convective motion associated with the squall line is proven by the intense lightning activity which is shown in Fig. 17b. From 06:00 UTC to 12:00 UTC more than 630 strikes overall were recorded by the lightningmaps.org network in the area that marks the

passage of the squall line.

The selected event was recorded by the two anemometers monitoring the La Spezia site (Table 1), whose location (i.e., SP 02 and SP 03) is shown in Fig. 3. Fig. 18 shows the time series of the slowly varying mean wind speed v and direction α recorded by these anemometers together with the abrupt change analysis. The order (from top to bottom) of the time series has been chosen to follow the chronological occurrence of this meteorological event. The anemometer SP 03, which is the closest to the sea, was the first to measure the wind speed increase that occurred around 07:51 UTC, as indicated by the vertical black dashed line in Fig. 18a. The anemometer SP 02, which is slightly farther from the coast, measured a more elevated ramp and peak at about 07:55 UTC, as indicated by the vertical black dashed line in Fig. 18c. The peak wind speed registered by the anemometers increases from the sea toward the land (i.e. from SP 03 to SP 02).

The abrupt change analysis in the standard deviation segments the signal duration of the slowly varying wind speed in 4 regions (3 changepoints). The same segmentation is then applied to the slowly varying mean wind direction. Region I (see Fig. 18) is characterized with roughly constant mean wind speed and direction. The mean wind speed and direction in the case of the anemometer SP 03 are respectively $v_b^- = 7.8$ m/s and $\alpha_b^- = 126°$, whereas in the case of the anemometer SP 02 they are respectively equal to $v_b^- = 5.9$ m/s and $\alpha_b^- = 126.3°$. These values of the mean wind speed and direction are identified with the low-level ABL wind prior to the downburst. Region II identifies the main peak due to the passage of the downburst event. In the case of SP 03 the main peak is characterized by $v_{max} = 18.5$ m/s at about 07:51 UTC and has a duration $\Delta t_{II} = 431\ s \simeq 7$ min. The slowly varying mean wind direction veered from about 125° (i.e. southeast) to $\alpha_{max} = 223.8°$ (i.e. southwest). As far as concerns the anemometer SP 02 the main peak of the recorded event reached $v_{max} = 23.3$ m/s at about 07:55 UTC and had a duration $\Delta t_{II} = 337\ s \simeq 6$ min. At maximum velocity the wind veered from about 125° to $\alpha_{max} = 197°$. Region III identifies a secondary low peak which has a duration of $\Delta t_{III} = 344\ s \simeq 6$ min in the case of SP 03 and a duration of $\Delta t_{III} = 847\ s \simeq 14$ min in the case of SP 02. The passage of the downburst event, as observed by the anemometers, lasts roughly $\Delta t_{tot} = 775\ s \simeq 13$ min in the case of SP 03 and $\Delta t_{tot} = 1184\ s \simeq 20$ min in the case of SP 02. Finally, region IV, which corresponds to the low-level ABL wind after the downburst passage, is characterized by $v_b^+ = 4.5$ m/s and $\alpha_b^+ = 148.4°$ in the case of SP 03 and $v_b^+ = 3.2$ m/s and $\alpha_b^+ = 165.1°$ in the case of SP 02. The sudden change in wind speed from region I to Region IV reported in Fig. 18 represents a transition between higher to lower wind speed regimes and is due to the passage of the squall line embedded in the cold front of Cyclone Klara. To see an appreciable change also in the wind direction due to the passage of the front, it is necessary to consider a time history longer than 1 h.

The main characteristics of the abrupt change in the standard deviation for this event are summarized in Table 8. It is worth mentioning that in this case the application of the abrupt change analysis considering as a statistics the mean produces almost the same results as the application of the abrupt change analysis in the standard deviation.

5.4. Reconstruction of the downburst event occurred in La Spezia on April 11, 2012

This time the parametric analysis has been carried out considering simultaneously two stations (i.e. SP 03 and SP 02) that registered the passage of the same downburst event. The low-level ABL wind speed and direction are determined according to the abrupt change analysis in the standard deviation. Accordingly, v_b is assumed to be the average between the ABL wind speed before and after the passage of the downburst cell considering both the stations, so it equals $v_b = 5.35$ m/s. The same procedure has been applied to the low-level ABL wind direction which is equal to $\alpha_b = 141.45°$. The parameters that minimize the *NMSE*, between the real measurements of the La Spezia downburst and the simulation are summarized in Table 9.

The downdraft radius in this case is $R = 505$ m and the radius at which the maximum velocity occurs is $R_{max} = 2 \cdot R = 1010$ m.

The results of the simulation and the comparison with the full-scale data are shown in Fig. 19, which confirms the ability of the proposed model to match simultaneously the wind profiles times series from two different anemometers that are recording the same event.

Considering the anemometer SP03 (Fig. 19, (a) and (b)), the simulated mean wind speed follows well the trend of the observed wind speed, however, the simulated main peak has a slightly longer duration than the recorded main peak. In this case the normalized means square error is $[NMSE(v)]_{SP03} = 0.085$. The simulated mean wind direction also shows a good correlation with the observed direction, there is however a slight detachment of the simulated mean wind direction in the region associated with the secondary low peak (i.e. from 1800 s up to 2100 s). The normalized error in this case is equal to $[NMSE(\alpha)]_{SP03} = 0.2238$.

Focusing now on the anemometer SP02 (Fig. 19, (c) and (d)), the simulated mean wind speed follows in a satisfactory way the recorded wind speed, however also in this case there is a slight overestimation of the duration of the main peak. The normalized error is equal to $[NMSE(v)]_{SP02} = 0.1138$. The simulated mean wind direction follows with minor detachment the observed wind direction during the ramp up interval (i.e. from 1500 to 1800 s). After this interval, from 1800 to 3000 s, the analytical model simulates the observed direction with a larger discrepancy. The authors believe that the orography of La Spezia, which is rather complex, could be the main cause of the inability of this model to simulate the thunderstorm outflow properly in the post-peak phase, when the outflow lands (see Fig. 20). The La Spezia site has a very complex orography indeed that can substantially perturb the downburst outflow, whereas the analytical model does not take these effects into consideration. The normalized error associated to the wind direction in this case is equal to $[NMSE(\alpha)]_{SP02} = 0.3913$. For this event the total normalized mean square error, considering both the anemometers, is equal to $NMSE = 0.8139$.

Fig. 20 shows the simulation of the horizontal mean wind speed at the height of the two anemometers at two snapshots in time which are indicated by the black dashed lines in Fig. 19. However, it should be noted that the two anemometers do not have the same height above the ground. In fact, the anemometer SP 02 is positioned at 10 m AGL while SP 03 is located at 13 m AGL. Since the analytical model reconstruct the wind field at a fixed height AGL, it is assumed for simplicity that the two anemometers have the same height (i.e. 10 m AGL).

The results of this simulation and, principally, the parameters that generated it (Table 9) provide a robust meteorological reconstruction of the downburst event recorded in La Spezia.

6. Conclusions and prospects

This paper proposes a novel analytical model that simulates the horizontal mean wind velocity at a fixed height above the ground, originating from a travelling downburst. The combined wind velocity is assumed to be a vector summation of three independent velocity fields, namely the radial impinging jet velocity, the translational velocity of the downburst cell and the low-level ABL wind velocity into which the downburst is embedded. A parametric analysis is developed and coupled with the analytical model to estimate the actual downburst's dimensions and relevant kinematic parameters of specific test cases according to a minimization function between simulation and measurements. A space-time reconstruction of two thunderstorm downburst events is carried out by means of coupled parametric-analytical model. The first downburst event occurred in the Port of Genoa and was triggered by an ordinary thunderstorm. In that case the reconstructed mean wind speed and direction by means of the parametric analysis matches the observed data to a very good extent reflected by a lower value of the NMSE. The second downburst event was caused by the passage of a squall-line

embedded in the cold front of the extra tropical cyclone that was passing over the Port area of La Spezia and was recorded by two anemometers (SP02 and SP03) located in different positions of the same area. In this case the analysis is carried out in order to reconstruct the time and space evolution of the downburst event as seen by the two anemometers. The result of the reconstruction and the comparison with the full-scale data confirm the ability of the proposed analytical model to match simultaneously the wind profiles time series from two different anemometers that are recording the same event. This is not an obvious outcome, especially considering that this thunderstorm is not an ordinary one but part of a complex and organized line of thunderstorms. Moreover, it is worth noting that, at the authors' knowledge, no other model has been used to reconstruct two concurrent anemometric time series (both speed and direction) before, which is thought to be an important advancement with respect to the models already available in the literature. The reconstructed mean wind speed and direction for the case of the anemometer SP03 shows a good correlation with the observed data, while the reconstruction of the anemometer SP02 shows some minor detachment in the simulation of the mean wind direction. One of the main reasons of this detachment is possibly due to the complex orography of the La Spezia site, which can substantially perturb the downburst outflows wind and is not included in the model yet.

This research opens up new perspectives and improvements that can be made to the model. The most important underlying hypothesis on which the model is based concerns the vector combination of the stationary downburst velocity, the translational velocity of the thunderstorm cell and the low-level ABL wind velocity. While using a vector combination of the stationary downburst velocity and translational velocity of the thunderstorm cell seems to be appropriate, the further vector combination with the low-level ABL wind velocity is quite questionable as pointed out by some preliminary wind tunnel experiments (Romanic and Hangan, 2018). In this regard, systematic laboratory tests have been recently conducted in the framework of the THUNDERR project (Solari et al., 2020) at the WindEEE Dome of the Western University. Second, until now the model is only two-dimensional. Further improvements of this model should incorporate the variation of the wind speed with the height AGL. Also, in this direction, the systematic analysis of downburst vertical profiles measured by LiDAR profilers is one of the main targets of the THUNDERR Project in order to clarify the time and height evolution of the velocity signals (Canepa et al., 2020). An important additional contribution should come from the LiDAR-Scanner (Windcube 400S) recently installed in the Port of Genoa. This scanner provides the reconstruction of the wind field on both the vertical and horizontal plane by taking the advantage of a wide and deep scanning resolution. The complementary use of the LiDAR-Scanner the LiDAR Profilers will offer a full picture of the storm physical behaviour at the ground, starting from the tracking of its touchdown position, storm propagation wind speed and direction, core dimension at near ground region and, also, shedding new lights on the interplay of the outflow embedded in the low-level ABL wind and the influence by the thunderstorm cell translation. Again in the framework of the THUNDERR Project, an attempt is currently in progress to couple radar and LiDAR measurements in order to obtain a robust reconstruction of the storm movement and the downdraft core dimension of the downburst; these are important model parameters and their knowledge can allow to reduce further the number of the parameters describing the model. Finally, another important aspect concerns the algorithm for the reconstruction of thunderstorm downburst events. The authors are working on a new global optimization algorithm based on meta-heuristic techniques that allows for code parallelization, which considerably reduces computational time and allows for better estimates of the parameters involved in the procedure.

Author contributions

The paper is part of the Ph.D. thesis of Andi Xhelaj whose supervisors are Prof. Giovanni Solari and Prof. Massimiliano Burlando. The initial draft of the paper was written by Andi Xhelaj. Prof. Massimiliano Burlando and Prof. Giovanni Solari made the first review. This gave rise to an iterative process leading to the final version of the paper with equal contributions.

Declaration of competing interest

The authors declare that they have no known competing financial interests or personal relationships that could have appeared to influence the work reported in this paper.

Acknowledgments

This research is funded by theg European Research Council (ERC) under the European Union's Horizon 2020 Research and Innovation Program (Grant agreement No. 741273) for the project THUNDERR – Detection, simulation, modelling and loading of thunderstorm outflows to design wind-safer and cost-efficient structures – supported by an Advanced Grant 2016. The data used for this research was recorded by the monitoring network set up as part of the European Projects Winds and Ports (grant No. B87E09000000007) and Wind, Ports and Sea (grant No. B82F13000100005), funded by the European Territorial Cooperation Objective, Cross-border program Italy-France Maritime 2007–2013.

References

Abd-Elaal, E.S., Mills, J.E., Ma, X., 2013a. An analytical model for simulating steady state flows of downburst. J. Wind Eng. Ind. Aerod. 115, 53–64.
Abd-Elaal, E.S., Mills, J.E., Ma, X., 2013b. A coupled parametric-CFD study for determining ages of downbursts through investigation of different field parameters. J. Wind Eng. Ind. Aerod. 123, 30–42.
Aboshosha, Haitham, Mara, Thomas, Case, Peter, 2017. New Framework for Estimating Thunderstorm Design Speed. In: Proceeding of the 13th Americas Conference on Wind Engineering. -.
Bendat, J.S., Piersol, A.G., 2010. Random Data: Analysis and Measurement Procedures, fourth ed.
Bjerknes, J., Solberg, H., 1922. Life Cycle of Cyclones and Polar Front Theory of Atmospheric Circulation, vol. 3. Geophysiks Publikationer, pp. 3–18.
Brooks, H.B., 1946. A summary of some radar thunderstorm observation. Bull. Am. Meteorol. Soc. 27, 557–563.
Burlando, M., 2019. Downburst outflow reconstruction by wind profile measurements. In: Proceedings of the 15th International Conference on Wind Engineering, p. A092704. September 1-6, Beijing, China.
Burlando, M., Romanic, D., Solari, G., Hangan, H., Zhang, S., 2017. Field data analysis and weather scenario of a downburst event in Livorno, Italy on 1 October 2012. Mon. Weather Rev. 145, 3507–3527.
Burlando, M., Zhang, S., Solari, G., 2018. Monitoring, cataloguing, and weather scenarios of thunderstorm outflows in the northern Mediterranean. Nat. Hazards Earth Sci. 18, 2309–2330.
Byers, H.R., Braham, R.R., 1949. The Thunderstorm: Final Report of the Thunderstorm Project. US Government Printing Office, Washington, DC.
Canepa, F., Burlando, M., Solari, G., 2020. Vertical profile characteristics of thunderstorm outflows. J. Wind Eng. Ind. Aerod. submitted for publication.
Chay, M.T., Albermani, F., Wilson, B., 2006. Numerical and analytical simulation of downburst wind loads. Eng. Struct. 28, 240–254.
Chen, L., Letchford, C., 2005. Proper Orthogonal Decomposition of two vertical profiles of full-scale nonstationary downburst wind speeds. J. Wind Eng. Ind. Aerod. 188, 61–79.
Chisholm, A.J., Renick, J.H., 1972. The kinematics of multicell and supercell Alberta hailstorms. In: Alberta Hail Studies. Research Council of Alberta HailStudies, Edmonton, Canada, pp. 24–31. Rep. 72–2.
Choi, E.C.C., Hidayat, F.A., 2002. Gust factors for thunderstorm and non-thunderstorm winds. J. Wind Eng. Ind. Aerod. 90, 1683–1696.
Davenport, A.G., 1961. The application of statistical concepts to the wind loading of structures. Proc. Inst. Civ. Eng. 19, 449–472.
De Gaetano, P., Repetto, M.P., Repetto, T., Solari, G., 2014. Separation and classification of extreme wind events from anemometric records. J. Wind Eng. Ind. Aerod. 126, 132–143.
Fujita, T.T., 1978. Manual of downburst identification for project NIMROD. SMRP Research Paper 156 - Chicago, IL: University of Chicago.
Fujita, T.T., 1981. Tornadoes and downbursts in the context of generalized planetary scales. J. Atmos. Sci. 38, 1511–1534.
Fujita, T.T., 1983. Andrews AFB Microburst. SMRP Research Paper 205.
Fujita, T.T., 1985. Downburst: Microburst and Macroburst. Univ. Chic. Press II, p. 122.
Fujita, T.T., 1990. Downburst: meteorological features and wind field characteristics. J. Wind Eng. Ind. Aerod. 36, 75–86.
Fujita, T.T., Wakimoto, R.M., 1981. Five scales of airflow associated with a series of downbursts on 16 July 1980. Mon. Weather Rev. 109, 1438–1456.

Glauert, M.B., 1956. The wall jet. J. Fluid Mech. 1, 625–643.
Hjelmfelt, M.R., 1988. Structure and life cycle of microburst outflows observed in Colorado. J. Appl. Meteorol. 27, 900–927 (August).
Holmes, J.D., Oliver, S.E., 2000. An empirical model of a downburst. Eng. Struct. 22, 1167–1172.
Huang, G., Zheng, H., Xu, Y., Li, Y., 2015. Spectrum models for non-stationary extreme winds. J. Struct. Eng. 141 (10), 04015010.
Ivan, M., 1986. A ring-vortex downburst model for flight simulations. J. Aircraft 23 (3), 232–236.
Jesson, M., Sterling, M., 2018. A simple vortex model of a thunderstorm downburst – a parametric evaluation. J. Wind Eng. Ind. Aerod. 174, 1–9.
Junayed, C., Jubayer, C., Parvu, D., Romanic, D., Hangan, H., 2019. Flow field dynamics of large – scale experimentally produced downburst flows. J. Wind Eng. Ind. Aerod. 188, 61–79.
Killick, R., Fearnhead, P., Eckley, I.A., 2012. Optimal detection of changepoints with linear computational cost. J. Am. Stat. Assoc. 107, 1590–1598.
Kim, J., Hangan, H., 2007. Numerical simulations of impinging jets with application to downbursts. J. Wind Eng. Ind. Aerod. 95, 279–298.
Lamb, O., 1895. Hydrodynamics. Dover, New York, p. 1932.
Lavielle, M., 2005. Using penalized contrasts for the change-point problem. Signal Process. 85, 1501–1510.
Le, T.-H., Caracoglia, L., 2017. Computer-based model for the transient dynamics of tall building during digitally simulated Andrews AFB thunderstorm. Comput. Struct. 193, 44–72.
Le, V., Caracoglia, L., 2018. Computationally efficient stochastic approach for the fragility analysis of vertical structures subjected to thunderstorm downburst winds. Eng. Struct. 165, 152–169.
Letchford, C.W., Mans, C., Chay, M.T., 2002. Thunderstorms – their importance in wind engineering (a case for the next generation wind tunnel). J. Wind Eng. Ind. Aerod. 90, 1415–1433.
Li, C., Li, Q.S., Xiao, Y.Q., Ou, J.P., 2012. A revised empirical model and CFD simulations for 3D axisymmetric steady-state flows of downbursts and impinging jets. J. Wind Eng. Ind. Aerod. 102, 48–60.
Lombardo, F.T., Smith, D.A., Schroeder, J.L., Metha, K.C., 2014. Thunderstorm characteristics of importance to wind engineering. J. Wind Eng. Ind. Aerod. 125, 121–132.
Marwitz, J.D., 1972. The structure and motion of severe hailstorms - Part II: multi-cell storms. J. Appl. Meteorol. 11, 180–188.
McCarthy, J., Wilson, J.W., Fujita, T.T., The Joint Airport Weather Studies Project, 1982. Bulletin of the American Meteorological Society 63, 15–22.
McCullough, M., Kwon, D.K., Kareem, A., Wang, L., 2014. Efficacy of averaging interval for nonstationary winds. J. Eng. Mech. 140 (1), 1–19.
Miguel, L.F.F., Riera, J.D., Fadel Miguel, L.F., 2018. Assessment of downburst wind loading on tall structures. J. Wind Eng. Ind. Aerod. 174, 252–259.
Mason, M.S., Wood, G.S., Fletcher, D.F., 2009. Numerical simulation of downburst winds. J. Wind Eng. Ind. Aerod. 97, 523–539.
Oseguera, R.M., Bowles, R.L., 1988. A simple analytic 3-dimensional downburst model based on boundary layer stagnation flow. NASA Tech. Memo. 100632.
Ponte Jr., J., Riera, J.D., 2007. Wind velocity field during thunderstorms. Wind Struct. 10, 287–300.
Poreh, M., Cermak, J.E., 1959. Flow characteristics of a circular submerged jet impinging normally on a smooth boundary. In: 6th Midwestern Conference on Fluid Mechanics Austin, Texas.
Proctor, F.H., 1987a. The terminal area simulation system - Part I: theoretical formulation. NASA Contractor Report 4046.
Proctor, F.H., 1987b. The terminal area simulation system - Part II: verification cases. NASA Contractor Report 4047.
Repetto, M.P., Burlando, M., Solari, G., De Gaetano, P., Pizzo, M., 2017. Integrated tools for improving the resilience of seaports under extreme wind events. Sustain. Cities Soc. 32, 277–294.
Repetto, M.P., Burlando, M., Solari, G., De Gaetano, P., Pizzo, M., Tizzi, M., 2018. A web-based GIS platform for the safe management and risk assessment of complex structural and infrastructural systems exposed to wind. Adv. Eng. Software 117, 29–45.
Rex, D.F., 1950. Blocking action in the middle troposphere and its effect upon regional climate. Tellus 2, 196–211.
Romanic, D., Hangan, H., 2018. The Interplay between Background Atmospheric Boundary Layer Winds and Downburst Outflows. A First Physical Experiment: Proceedings of the XV Conference of the Italian Association for Wind Engineering (IN-VENTO 2018). Elsevier, Napoli, Italy.
Romanic, D., LoTufo, J., Hangan, H., 2019a. Transient behaviour in impinging jets in crossflow with application to downburst flows. J. Wind Eng. Ind. Aerod. 184, 209–227.
Romanic, D., Nicolini, E., Hangan, H., Burlando, M., Solari, G., 2019b. A novel approach to scaling experimentally produced downburst-like impinging jet outflows. J. Wind Eng. Ind. Aerod. 196.
Riera, J.D., 2019. Design criteria for downburst induced wind loading. In: Proceedings of the 15th International Conference on Wind Engineering. -.
Romanic, D., Chowdhury, J., Chowdhury, J., Hangan, H., 2020. Investigation of the transient nature of thunderstorm winds from Europe, United States and Australia through detection of abrupt changes in wind speed records. Mon. Weather Rev. 148 (9), 3747–3771.
Schultz, T.A., 1990. Multiple vortex ring model of the DFW microburst. J. Aircraft 27 (2), 163–168.
Solari, G., 2014. Emerging issues and new frameworks for wind loading on structures in mixed climates. Wind Struct. 19, 295–320.
Solari, G., Burlando, M., De Gaetano, P., Repetto, M.P., 2015. Characteristics of thunderstorms relevant to the wind loading of structures. Wind Struct. 20, 763–791.
Solari, G., Burlando, M., Repetto, M.P., 2020. Detection, simulation, modelling and loading of thunderstorm outflows to design wind-safer and cost-efficient structures. J. Wind Eng. Ind. Aerod. 200.
Solari, G., Repetto, M.P., Burlando, M., De Gaetano, P., Pizzo, M., Tizzi, M., Parodi, M., 2012. The wind forecast for safety and management of port areas. J. Wind Eng. Ind. Aerod. 104–106, 266–277.
Solari, G., 2019. Wind Science and Engineering. Springer, Switzerland.
Solari, G., 2020. Thunderstorm downburst and wind loading of structures: progress and prospect. Front. Built Environ. 6 (63), 1–24.
Su, Y., Huang, G., Xu, Y., 2015. Derivation of time-varying mean for non-stationary downburst winds. J. Wind Eng. Ind. Aerod. 141, 39–48.
Tubino, F., Solari, G., 2020. Time varying mean extraction for stationary and nonstationary winds. Wind Engineering & Industrial Aerodynamics.
Vicroy, D.D., 1991. A simple, analytical, axisymmetric microbust model for downdraft estimation. NASA Technical Memorandum 104053.
Vicroy, D.D., 1992. Assessment of microburst models for downdraft estimation. J. Aircraft 29, 1043–1048.
Wilson, J.W., Roberts, R.D., Kessinger, C., McCarthy, J., 1984. Microburst wind structure and evaluation of Doppler radar for airport wind shear detection. J. Clim. Appl. Meteorol. 23, 898–915.
Wood, G.S., Kwok, K.C.S., 1998. An empirically derived estimate for the mean velocity profile of a thunderstorm downburst. In: 7th Australian Wind Engineering Society Workshop Auckland. New Zealand.
Wood, G.S., Kwok, K.C.S., Motteram, N.A., Fletcher, D.F., 2001. Physical and numerical modelling of thunderstorm downburst. J. Wind Eng. Ind. Aerod. 89, 535–552.
Xu, Z., Hangan, H., Yu, P., 2008. Analytical solutions for a family of Gaussian impinging jets. J. Appl. Mech. 75, 021019-1-02101912.
Zhang, S., Solari, G., De Gaetano, P., Burlando, M., Repetto, M.P., 2018. A refined analysis of thunderstorm outflow characteristics relevant to the wind loading of structures. Probabilist. Eng. Mech. 54, 9–24.
Zhang, S., Solari, G., Burlando, M., Yang, Q., 2019. Directional decomposition and properties of thunderstorm outflows. J. Wind Eng. Ind. Aerod. 189, 71–90.